UC Berkeley
UC Berkeley Previously Published Works

Title
Synthetic approaches for thin-film halide double perovskites

Permalink
https://escholarship.org/uc/item/9rc0h8hq

Journal
Matter, 4(6)

ISSN
2590-2393

Authors
Zhao, Yihui
Cruse, Kevin
Abdelsamie, Maged
et al.

Publication Date
2021-06-01

DOI
10.1016/j.matt.2021.03.009

Peer reviewed

eScholarship.org Powered by the California Digital Library
University of California

Synthetic Approaches for Thin Film Halide Double Perovskites

Yihui Zhao,[a] Kevin Cruse,[a,b] Maged Abdelsamie,[a] Gerbrand Ceder,[a,b] Carolin M. Sutter-Fella[c,d*]

[a] Materials Sciences Division, Lawrence Berkeley National Laboratory, Berkeley, CA, USA

[b] Department of Materials Science and Engineering, University of California, Berkeley, CA, USA

[c] Chemical Sciences Division, Lawrence Berkeley National Laboratory, Berkeley, CA, USA

[d] Molecular Foundry Division, Lawrence Berkeley National Laboratory, Berkeley, CA, USA

* corresponding author: csutterfella@lbl.gov

Abstract

Inspired by the fascinating class of hybrid organic-inorganic halide perovskite materials, halide double perovskites have emerged as non-toxic Pb-free contender for the application as active layers in optoelectronic devices. Heterovalent substitution of Pb^{2+} by non-toxic metal cations yield the double perovskite structure which allows for compositional flexibility. In fact, the compositional space is large given that multiple cations and halides can be combined resulting in $>10^6$ perovskite combinations. A starkly increasing number of stable halide double perovskite compositions are theoretically predicted. The synthesis however, lacks behind and many double perovskites are primarily synthesized as powder samples instead of thin films. The latter however, are needed for thin film devices such as solar cells, light-emitting devices, and thin film transistors. When comparing the synthetic approaches successfully applied to hybrid perovskites to methods used for the fabrication of double perovskites, the latter is clearly in its very infancy. The question is whether solution engineering and compositional modification strategies can be exploited to match the exceptional optoelectronic properties of hybrid perovskites. This review is motivated by a text mining effort that not only illustrates the prevalence of powder over thin film synthesis but also the discrepancy between the number of compositions experimentally realized and studied as compared to the many predicted compositions. Here we summarize the synthesis aspects of halide double perovskites, and in particular of thin films, including deposition techniques and synthetic modifications to alter film properties.

1. Introduction

Developing materials for renewable energy generation has attracted significant research effort so as to answer the global climate change caused by combustion of fossil fuels. Hybrid organic-inorganic Pb-halide perovskites with the protagonist $CH_3NH_3PbI_3$ ($MAPbI_3$) and general formula ABX_3 (A is a monovalent cation, B is a divalent metal cation, and X is a halide anion, Cl, Br, I, or a combination thereof, see Figure 1) have sparked enormous research interest (reflected by the rise in number of publications/year, illustrated in Figure 2A) due to their intriguing properties. Within only a decade, the power conversion efficiency (PCE) of perovskite solar cells (PSCs) has increased from 3.8% in 2009[1] to 25.5% in 2021 in single-junction architectures,[2] and to 29.5% in silicon-based tandem cells,[2] exceeding the maximum efficiency achieved in single-junction silicon solar cells. These achievements are due to their extraordinary optoelectronic properties, including strong and tunable light absorption/emission, long carrier diffusion lengths, and high carrier mobilities.[3–8] In addition to inexpensive source materials, halide perovskite films are typically prepared by inexpensive chemical solution processing including spin coating and roll-to-roll compatible printing techniques.[9,10] Despite these advantages, hybrid halide perovskites are currently limited by poor stability in ambient conditions and lead toxicity. So far, significant efforts have been made to address the stability issues in ABX_3 perovskites, including compositional engineering,[11–13] dimensional engineering,[14] organic substitution[15] and device encapsulation.[16] It is believed that stability will meet industry standards upon further improvements.[17] On one hand, the toxicity of Pb is a serious concern for the health and the environment and needs to be eliminated in a sustainable technology,[17] on the other hand, its electron configuration is part of the success of

ABX_3, i.e. its extraordinary optoelectronic properties.[7] In this regard, a Pb-free alternative should seek to deploy similar elements with lone-pair *s* electrons. Thus, replacement of Pb^{2+} by other divalent cations e.g., germanium (Ge^{2+})[18,19] or tin (Sn^{2+})[20,21] is an obvious approach but limited by their oxidation to more stable 4+ oxidation states[22] and therefore limited PCE of less than 10%.[18,23–27] Consequently, researchers have focused on derivatives of the perovskite family in their search for lead-free stable alternatives which may be summarized according to structure and valence state of the metal cation as illustrated in Figure 1. Layered/dimer perovskites, $A_3B^{3+}{}_2X_9$, with substitution of Pb^{2+} by isoelectronic and non-toxic bismuth (Bi^{3+}) only form 0D or 2D structures that suffer from high exciton binding energy, short carrier diffusion length, high trap state density, and low charge carrier mobility, which results in poor device performance.[28–34] Another example in the layered/dimer perovskite category is replacement of Pb^{2+} with Sb^{3+}, e.g. $Cs_3Sb_2I_9$[35] and $Rb_3Sb_2I_9$[36]. When the A-site is occupied by a large organic cation, such as methylammonium ($CH_3NH_3^+$, MA), the structure can transform into zero-dimensional dimers of facesharing BX_6 octahedra, e.g. $MA_3Sb_2I_9$[37] and $MA_3Bi_2I_9$[31–33,38]. The tetravalent-metal vacancy ordered double perovskites ($A_2B^{4+}X_6$) are a structural derivative of the archetypal perovskite (ABX_3) structure, where half of the tetravalent atoms is removed and replaced by a vacancy. $A_2B^{4+}X_6$ compounds have a close-packed anionic lattice similar to ABX_3 perovskites, and exhibit several similar optoelectronic properties. Cs_2SnI_6, for example, has a direct bandgap as low as ~1.3 eV and moreover good stability in air and moisture due to the stable +4 oxidation state of Sn.[39] Similarly, $Cs_2TiI_2Br_4$ and Cs_2TiBr_6 have bandgaps of ~1.38 and ~1.78 eV, which are suitable for single-junction PSCs and tandem photovoltaic application, respectively.[40] Finally, in the mixed double perovskite category ($A_2B^+B'^{3+}X_6$), two Pb^{2+} metals are replaced by a pair of metals with oxidation states +1 and +3 to maintain charge neutrality.[41–45] One of the pioneer compounds of lead-free halide double perovskites is $Cs_2AgBiBr_6$ which exhibits an indirect bandgap of 1.95 eV and a notably long photoluminescence (PL) lifetime of ~660 ns at room temperature.[43] This lifetime is higher than the lifetime of high-quality pure Br $MAPbBr_3$ films (170 ns)[46]. In addition, unlike Pb-based perovskites that have to be synthesized in the glovebox, $Cs_2AgBiBr_6$ shows high stability, which allows it to be synthesized under ambient conditions.[43,44] Apart from $Cs_2AgBiBr_6$, other members of this perovskite-derived class of materials have been predicted with high stability and good optoelectronic properties, including $Cs_2InSbCl_6$, $Cs_2AgInBr_6$, $Rb_2AgInBr_6$, and $Rb_2CuInCl_6$.[47–49] In the quest for Pb-free perovskites with multiple cations on the A and B sites as well as multi halides, there are $>10^6$ perovskite combinations.[50] Few of these have been actually synthesized as shown in Figure 2B. This Figure lists all halide double perovskites that have been synthesized so far and were compiled by a text mining effort screening materials science literature for "perovskite(s)" followed by formulae-analysis tools to narrow down on articles concerned with halide stoichiometry equal to 6, corresponding to $A_2BB'X_6$ (more details can be found in the caption of Figure 2). It is noted that the search term "elpasolite" returns an additional 284 articles but these are mostly concerned about rare-earth metals / lanthanide compounds which are not considered here. Three-dimensional (3D) $A_2B^+B'^{3+}X_6$ can be further broadened to lower dimensional perovskites by relaxing structural constraints and thereby increasing design flexibility and tuneability of functional properties. For example, by occupying the A-site with a too large organic cation, a two-dimensional (2D) structure can be formed.[51]

Despite the promise of non-toxic perovskite-derived compounds with enhanced stability, halide double perovskites are currently not achieving similar performance as $APbX_3$-based devices and they lack behind significantly when comparing the dynamics of the field reflected by the number of publications per year (Figure 2A). A few studies have been undertaken to understand the performance challenges of different double perovskite compounds that were synthesized so far.[52,53] Regardless of the long carrier lifetime in $Cs_2AgBiBr_6$, films were found to suffer from fast recombination at the surface which likely limits their performance at the current stage.[52]

Here, in this review we specifically focus on the synthetic aspects of halide double perovskites, including techniques and synthetic modifications to improve and tailor film quality. Given the combinatorial interplay of elements A, B^+, B'^{3+} and X, the compositional space of Pb-free halide perovskite derivatives is large and phase pure synthesis of high quality compounds is still in its infancy.[28,45,50,54–56] In this regard exploration of synthetic strategies can provide a powerful approach to enhance material properties and thus, device performance. Motivated by a text mining effort on existing literature, section 2 of this review summarizes and discusses synthesis strategies divided into crystal and thin film synthesis. This is followed by strategies for how to improve film quality in section 3. We compare resulting properties of double perovskites correlated to synthesis method, and devices. In section 4, compositional engineering at the B-, B'-, and X-sites as well as dimensional reduction with a focus on synthetic aspects are summarized. Finally, in section 5, synthetic challenges are discussed and we provide perspectives for future directions in the field of double perovskites. It is noted that there are several extensive and excellent review papers that provide a broader overview and state of the art of the field.[49,56,57]

2. Lead-free halide double perovskite synthesis

When entering the field of Pb-free halide double perovskites it becomes apparent that synthesis is more complex given the quaternary nature of the compounds, lower precursor solubility, and the need for higher annealing temperatures, as compared to ABX_3 perovskites, to obtain phase pure and high-quality materials. Figure 2B illustrates an overview of synthetic approaches to fabricate crystals or thin films using solution synthesis/solid state synthesis or vapor deposition/solution deposition, respectively, differentiated by material composition. The text mining techniques used to compile and sort publications are described in the figure's caption. Clearly, $Cs_2AgBiBr_6$ has by far been the most synthesized material from this class followed by Cs_2SnI_6. In the following section, we give details on the most commonly used deposition techniques divided into their final physical state, that is crystal versus thin film. In contrast to ABX_3 perovskites, many synthetic approaches focus on crystal instead of thin film synthesis which in part can be explained by material complexity and limited precursor solubility. Here, the focus is on double perovskite thin films because one of the motivating factors for research on the Pb-free double perovskites was the replacement of $APbX_3$ which attracted significant interest as active layer in thin film optoelectronics. Table 1 provides an overview of synthetic approaches and synthesis conditions for different double perovskite compositions.

Table 1. Preparation and synthesis conditions of halide double perovskite compounds differentiated by their physical appearance.

Crystal

Compound	Synthesis	Synthesis	Heating	Year &

	method	**Atmosphere**	**condition**	**Reference**
Cs_2BiAgX_6 (X=Br or Cl)	Solid-state reaction	Ambient air	210°C for 10 h	2016[44]
Cs_2BiAgX_6 (X=Br or Cl)	Solid-state reaction	Vacuum (10^{-3} Torr)	Heating to 500°C over 5h, annealing for 4h	2016[41]
$Cs_2AgSbCl_6$	Solid-state reaction	Evacuated ampoules	210°C for 5 days	2017[62]
$Cs_2AgInCl_6$	Solid-state reaction	Evacuated ampoules	400°C for 5 days	2017[62]
$Cs_2AgSb_xIn_{1-x}Cl_6$	Solid-state reaction	Evacuated ampoules	300°C for 6 days	2017[62]
$Cs_2Ag(Bi_{1-x}M_x)Br_6$ (M=In, Sb)	Solid-state reaction	Vacuum	320°C for 20 h	2017[63]
$Cs_2TiI_xBr_{6-x}$	Solid-state reaction	Vacuum (10^{-6} Torr)	Heating to 700°C by 10°C/min, annealing for 72 h, cooling to RT by 10°C/min	2018[40]
Cs_2NaVCl_6	Solid-state reaction	Vacuum	550°C for 20 h	2019[64]
$Cs_2AgBiBr_6$	Solution processing	Ambient air	110°C for 2 h	2016[43]
Cs_2BiAgX_6 (X=Br or Cl)	Solution processing	Ambient air	120°C	2016[44]
$Cs_2AgBiBr_6$	Solution processing	Ambient air	110°C for 2 h, cooling to 80°C for 6 h	2017[65]
$Cs_2AgSbCl_6$	Solution processing	Ambient air	80°C, Drying at 150°C for 7 h	2017[66]
$Cs_2InAgCl_6$	Solution processing		Heating at 115°C for 30 min	2017[42]
$Cs_2AgBiBr_6$	Solution processing	Ambient air	120°C for 3 h, cooling to 100°C by 2°C/h, cooling to 50°C by 1°C/h	2018[67]
$Cs_2AgBiBr_6$	Solution processing	Ambient air	150°C, cooling to RT by 10°C/h	2018[68]
$Cs_2AgBiBr_6$	Solution processing	Ambient air	Evaporated at 60°C and 150°C	2020[69]
$Cs_2SbAgCl_6$	Solution processing		120°C for 2 h, Cooling to RT over 2 h	2018[70]
$Cs_2Ti(Br_xCl_{1-x})_6$	Solution processing	Ar	RT	2020[71]
Cs_2MInCl_6:xSb (M = Na, K)	Solution processing		Heating at 100°C	2020[72]
Bi^{3+}-Er^{3+}/Bi^{3+}-Yb^{3+} doped $Cs_2AgInCl_6$	Solution processing		Heating at 80°C for 20 min	2020[73]

Mn doped $Cs_2AgInCl_6$	Solution processing		Heating at 72°C	2018[74]
Cs_2SnI_6	Hot injection	Vacuum	Heating at 120°C for 1 h 220°C for injection	2016[75]
Cs_2AgBiX_6 (X = Cl, Br)	Hot injection	Vacuum & N_2	110°C in vacuum for 45 min, 140°C in N_2 for injection	2018[76]
$Cs_2AgBiBr_6$	Hot injection	Vacuum & N_2	120°C in vacuum for 30 min, 145°C in N_2 for injection	2020[77]
$Cs_2Na_{1-x}Ag_xBiCl_6$	Hot injection	N_2	Heating at 140°C	2020[78]
$(MA)_2AgBiBr_6$	Hydrothermal		433 K for 3 days, cooling to RT in 3 h	2017[79]
$(MA)_2KBiCl_6$	Hydrothermal		423 K	2016[80]
$Cs_2AgInCl_6$	Hydrothermal		180°C, cooling to RT by 0.5°C/h	2018[81]
$Cs_2Ag_xNa_{1-x}InCl_6$	Hydrothermal		180°C for 12 h, cooling to 50°C by 3°C/h	2018[82]
$Cs_2AgSbBr_6$	Hydrothermal		160°C for 5 days	2019[83]
Cs_2NaBiI_6	Hydrothermal		120°C for 2 h, cooling to RT over 12 h	2018[84]
$Cs_2NaBi_{1-x}In_xCl_6$	Hydrothermal		453 K for 12 h	2019[85]
Cs_2SnCl_6:Bi	Hydrothermal		180 °C for 10 h cooling to RT over 20 h	2018[86]

Thin film

Compound	Deposition method	Synthesis atmosphere	Heating condition	Year & Reference
$Cs_2AgBiBr_6$	Sequential vapor deposition	Vacuum 1×10^{-3} Pa	2 step post-annealing 200°C for 5 h + 240°C for 5 h	2018[87]
$Cs_2AgBiBr_6$	Single source vapor deposition	Vacuum 5×10^{-4} Pa	Post-annealing 300°C for 15 min in N_2	2019[88]
$Cs_2AgBiBr_6$	Sequential vapor deposition	Vacuum 5×10^{-4} Pa	Post-annealing 220°C for 30 min	2019[89]
$Cs_2AgBiBr_6$	Sequential vapor deposition	Vacuum	250 ºC for 30 min in air	2020[90]
Cs_2TiBr_6	Sequential vapor deposition		In $TiBr_4$ vapor Annealing 200°C for 24 h	2018[91]
Cs_2SnI_6	Sequential vapor deposition	CsI in Vacuum $\sim5\times10^{-7}$	Annealing CsI film for 20−40 min at 190°C in SnI_4 vapor	2016[92]

		Torr; SnI4 in N_2		
Cs_2SnI_6	Aerosol-assisted chemical vapor deposition		Post-annealing 150°C for 30 min in ambient air	2018[93]
$Cs_2Ag_xNa_{1-x}InCl_6$	Sequential vapor deposition	Vacuum 6×10^{-6} mTorr	Post-annealing 150 °C for 5 min in N_2	2018[82]
$Cs_2AgBiBr_6$	Spin-coating	Ambient air	Preheating at 75°C, Post-annealing 285°C for 5 min	2017[94]
$Cs_2AgBiBr_6$	Spin-coating	Low-pressure assisted, 20 Pa	Post-annealing 250°C for 10 min	2018[95]
$Cs_2AgBiBr_6$	Spin-coating	N_2	Post-annealing 250°C for 5 min	2018[96]
$Cs_2AgBiBr_6$	Spin-coating	Vacuum	Preheating substrate at 75°C, Post annealing at 250°C	2018[97]
$Cs_2AgBiBr_6$	Spin-coating		Preheating solution at 70°C, Post-annealing 280°C for 5 min	2018[98]
$Cs_2AgBiBr_6$	Spin-coating	Glovebox, Low-pressure assisted, 5 Pa	Preheating solution at 80°C, Post-annealing 285°C for 5 min	2018[99]
$Cs_2AgBiBr_6$	Spin-coating		Post-annealing 250°C for 20 min	2018[100]
$Cs_2AgBiBr_6$	Spin-coating	Ambient air	Post-annealing 280°C for 5 min	2019[89]
$Cs_2AgBiBr_6$	Spin-coating		Preheating solution at 70°C, Post-annealing 250°C for 10 min	2019[101]
$Cs_2AgBiBr_6$	Spin-coating		Solution prepared at 150°C, Post-annealing 250 °C for 10 min.	2019[102]
$Cs_2AgBiBr_6$	Spin-coating		Preheating solution at 50°C, Post-annealing 280°C for 5 min	2019[103]
$Cs_2AgBiBr_6$	Spin-coating	Ambient air	Preheating solution at 80°C, Post-annealing 280°C for 5 min	2020[104]
$Cs_2AgBiBr_6$	Spin-coating	N_2	Preheating solution at 80°C, Post-annealing 285°C for 5 min	2020[105]
$Cs_2AgBiBr_6$	Spin-coating	Glovebox	Post-annealing 320°C for 5 min	2020[106]
$Cs_2AgBiBr_6$	Spin-coating	Glovebox	Post-annealing 210°C	2020[107]
$Cs_2AgBiBr_{6-2x}S_x$	Spin-coating	Glovebox	Preheating at 70°C for 10 min,	2020[108]

			Post-annealing 280°C for 10 min	
$(Cs_{1-x}Rb_x)_2AgBiBr_6$	Spin-coating	low pressure assisted, 20 Pa	Post-annealing 250 °C for 10 min	2019[109]
$Cs_2AgSbBr_6$	Spin-coating		Preheating at 200°C, Post-annealing 150°C for 30 min	2019[83]
$Cs_2AgSb_xBi_{1-x}Br_6$	Dip-coating	Ar	Dissolving at 180°C, Post annealing at 250°C for 0.5 h	2019[110]
Cs_2PtI_6	Doctor blade	Ambient air	Preheating substrate at 70°C, Post-annealing at -15°C in Hg and 100°C in vacuum for 1 h	2020[111]
$Cs_2SnI_{6-x}Br_x$	Electro-spraying CsI + Drop coating SnI_4	Ambient air	Post-annealing, CsI film 300°C for 30 min; SnI_4 film 110°C for 20 min in air	2017[112]

2.1 Crystal synthesis

Crystal synthesis is a starting step for some approaches targeting thin film fabrication and therefore, is briefly discussed in the following. The crystal synthesis described includes macroscopic single crystals, polycrystalline powders and nanocrystals and is classified into two routes, i.e. solid-state reaction and solution-based processing (compare Figure 3). With solution-based processing we refer to any synthesis that involves a starting chemical precursor solution where some or all elements of the final compound are dissolved or dispersed in a solvent. As these synthesis routes apply to many compositions of the perovskite-derived material class, we describe examples limited to $A_2B^{+}B'^{3+}X_6$ compounds.

2.1.1 Solid-state route

One of the pioneers, Volonakis et al. synthesized $Cs_2AgBiCl_6$ crystals via solid-state reaction in sealed ampoules.[41] The sequence of this reaction is described in Figure 3A where CsCl, $BiCl_3$ and AgCl are mixed first in a molar ratio of 2:1:1, and then the mixture is loaded to a fused silica ampoule that is flame sealed under vacuum. Next, the sealed ampoule is gradually heated to 500℃ over the course of 5 hours and annealed for another 4 hours. After cooling to room temperature, yellow polycrystalline $Cs_2AgBiCl_6$ powder forms consisting of octahedrally shaped single crystals with ~0.1 mm length. McClure et al. reported a different solid-state reaction method for the synthesis of polycrystalline Cs_2AgBiX_6 (X=Cl or Br) powder, which is processed in air and at a relatively low temperature.[44] As summarized in Figure 3B, the starting materials CsX, BiX_3 and AgX were firstly ground together for 20 min and then transferred into an alumina crucible. Then the mixture was heated in a box furnace in air at 210°C for 10 h. After at least two cycles of grinding-heating, nearly phase pure polycrystalline Cs_2AgBiX_6 was obtained. It was found that the $Cs_2AgBiBr_6$ phase only appeared after heating to 150 °C. In stark contrast, $Cs_2AgBiCl_6$ phase was detected upon room temperature grinding of the reactants. The authors attributed the reason to the hygroscopicity of $BiCl_3$ facilitating the reaction of the reagents.

2.1.2 Solution-based routes

Slavney et al. and McClure et al. were the first to prepare $Cs_2AgBiBr_6$ and Cs_2AgBiX_6 (X = Cl, Br) crystals, respectively, via a solution-based method.[43,44] Slavney et al. used CsBr, $BiBr_3$ and AgBr in a ratio of 2:1:1 as starting materials dissolved in HBr solution heated to 110 °C for 2 hours (compare Figure 3C).[43] After cooling to room temperature with a cooling rate of 2 °C/hr, an orange powder identified as $Cs_2AgBiBr_6$ precipitated from the solution which was subsequently filtered and dried. By reducing the cooling rate to 1 °C/hr, larger single crystals (shown in Figure 3C) were obtained. It was stated by the authors that this solution-based approach is challenging due to the insolubility of AgBr.[43]

McClure et al. used a precipitation approach from mixed solvents (hydrohalic and hypophosphorous acid) heated to 120 °C and compared samples made via solid-state and solution routes.[44] The results showed that only the solution synthesis approach yielded phase pure material. In addition, it can be performed at lower temperature than the solid-state synthesis which is possibly linked to the fact that dissolved molecular building blocks require a lower thermal activation compared to mechanically ground powders.

Zhang et al. reported a one-step hydrothermal process for synthesis of Cs_2NaBiI_6 crystals (Figure 3D).[84] As starting materials, CsI, NaI and BiI_3 were dissolved at a stoichiometric molar ration of 2:1:1 in HI acid. After the solution was transferred to an autoclave it was heated to 120°C for 2 h. Dark cerise Cs_2NaBiI_6 crystals were obtained after cooling to room temperature over 12 h. Excess reactants were removed by washing with deionized water, followed by drying in a vacuum chamber.

As a last example, Figure 3E shows the sequence of a synthesis route for Cs_2AgBiX_6 nanocrystals via hot injection, as reported by Creutz et al.[76] In this approach, Cs(OAc), Ag(OAc) and $Bi(OAc)_3$ were dissolved in a mixture of octadecene, oleic acid and oleylamine, followed by heating to 110°C under vacuum for 45 min. Then the obtained solution was heated to 140 °C under a nitrogen atmosphere and TMSX (TMS = trimethylsilyl, X = Cl or Br) was injected. After centrifugation of the solution and extraction of the precipitate using a small amount of toluene, homogenous and cube-shaped Cs_2AgBiX_6 nanocrystals were obtained (compare TEM image of $Cs_2AgBiBr_6$ nanocrystals in Figure 3D). Interestingly, thermodynamically driven postsynthetic anion-exchange reactions were performed at room temperature to convert $Cs_2AgBiBr_6$ nanocrystals to Cs_2AgBiI_6 nanocrystals, and $Cs_2AgBiCl_6$ to $Cs_2AgBiBr_6$.[76]

Very similar methods with little or without modifications from aforementioned routes used have been reported for the synthesis of broad class of lead-free halide double perovskites.[62,65,82,94,96,108,113–119]

2.2 Thin film synthesis

Now, we focus our attention on thin film synthesis. From a technological standpoint many optoelectronic devices rely on the integration of active thin films such as in solar cells, transistors, and light-emitting devices. To date, vapor and solution deposition are the two most popular routes that have been successfully used to prepare halide double perovskite thin films.

2.2.1 Solution deposition

Chemical solution deposition is a low-cost fabrication method that is extensively used for the fabrication of ABX_3 thin films.[9] It allows for large area scale up, for example by printing precursor inks. Another advantage is the facile control of the final stoichiometry and the possibility of compositional alloying by directly adding desired elements to the precursor solution. Limitations of solution deposition include dependence on precursor solubility, purity, and incomplete removal of organic and other residues.

In analogy to the widely used one-step solution synthesis of halide perovskites[9] a typical one-step process for the fabrication of Cs_2AgBiX_6 (X = Br or Cl) thin films is illustrated in Figure 4A. The starting precursor is prepared by either dissolving pre-synthesized Cs_2AgBiX_6 crystals[41,95,96,100,102,103,107,115] or by dissolving binary metal halide precursors CsX, AgX and BiX_3 (typically in a molar ratio of 2:1:1)[94,97,99,104]. The low precursor solubility has hampered the one-step solution deposition of Cs_2AgBiX_6. The solubility of the double perovskite precursors can be ~one order of magnitude lower than typical concentrations used for the synthesis of ABX_3 via solution synthesis.[94] Greul et al. screened several solvents for their solubility of AgBr, CsBr, $BiBr_3$, and $Cs_2AgBiBr_6$ crystals, and found that dimethyl sulfoxide (DMSO) shows the highest solubility of ~0.6 M compared to ~0.1 M in N,N-Dimethylformamide (DMF) and N-Methyl-2-pyrrolidone (NMP).[94] The DMSO-based $BiBr_3$+AgBr+CsBr precursor solution was spin-coated onto the substrate followed by annealing at temperatures ≥ 250 ℃ to form phase pure $Cs_2AgBiBr_6$ without the secondary phases AgBr and $Cs_3Bi_2Br_9$.[94] Note that density functional theory (DFT) calculations show that the stable chemical potential region for phase pure $Cs_2AgBiBr_6$ is narrow.[121] Synthetic modifications of solution synthesis to enhance film quality are summarized in section 3.

Liu et al. fabricated Sb alloyed $Cs_2AgBiBr_6$ films using a dip-coating method (Figure 4B).[110] In this process, CsBr, AgBr, $SbBr_3$ and $BiBr_3$ powders were dissolved first in DMSO under heating at 180 ℃. Then a frosted quartz slide substrate was dipped into the precursor solution for ~5 s, then taken out slowly, followed by holding it above a hot plate set to 250 ℃ to gently remove the DMSO solvent before it was placed on the hotplate to form the $Cs_2AgSb_xBi_{1-x}Br_6$ thin film.

In analogy to ABX_3 synthesis via a two-step process which employs formation of a solid PbI_2 film that is converted by reaction with MAI,[9] Lee et al. reported a two-step solution deposition for Cs_2SnI_6 thin films, where the first step is the CsI deposition followed by a SnI_4 treatment in step two (Figure 4C).[112] CsI was dissolved in a mixture of water and 2-isopropyl alcohol (IPA) and deposited by three different processes (spin-coating, drop-coating and electro-spraying). Interestingly, each coating process resulted in different microstructures, i.e. CsI clusters for spin-coating, dendrites for drop-coating, and CsI thin film morphology for electro-spraying. In step two, a solution of SnI_4 in EtOH was used to react with the CsI layer to form Cs_2SnI_6. The results showed that, Cs_2SnI_6 films are more compact and have a smoother surface when CsI is deposited via electro-spraying. This study amplifies that it is necessary to optimize and control starting morphology in the first step because it can affect the second step significantly.

2.2.2 Vapor deposition

Vapor deposition is widely used for the fabrication of thin film semiconductors, and has also been successfully used for ABX_3 perovskites.[122] It offers the opportunity to overcome some of the limitations of solution deposition including limited precursor solubility and closely related, achievable film thickness.[87] Figure 5A illustrates a sequential vapor deposition process for $Cs_2AgBiBr_6$ films, reported by Wang et al.[87] The deposition was carried out by first evaporating AgBr onto the substrate, then $BiBr_3$ and CsBr sequentially on top of the film using a rotating substrate holder in vacuum. A crystalline $Cs_2AgBiBr_6$ film was obtained by a two-step post annealing process in air, first at 200℃ for 5 hours, which resulted in the formation of the double perovskite phase, and second at 240℃ for 5 hours to increase crystallinity. It was found that a stoichiometric molar ratio of binary halide precursors (2:1:1 of CsBr:AgBr:$BiBr_3$) results in impurity phases while an excess of $BiBr_3$ results in close to phase pure $Cs_2AgBiBr_6$ films. This method resulted in 380 nm thick films and a PCE of 1.37%. The devices demonstrated high stability under ambient conditions, where the PCE was maintained at 90% after 240 h of air-storage. As an alternative method, single-source evaporation, using a pre-prepared $Cs_2AgBiBr_6$ crystal powder as the evaporation source, was carried out by Fan et al. (Figure 5B).[88] The best post deposition annealing condition was found at 300℃ for 15 min resulting in phase pure (i.e. no co-presence of e.g. $CsAgBr_2$, $Cs_3Bi_2Br_9$, and AgBr), uniform, and smooth films with grain sizes up to a few hundred nanometers. As a result, an optimal PCE of 0.7% was obtained from the solar cell devices based on the synthesized $Cs_2AgBiBr_6$ films. In a vapor-based method that makes use of diffusion control, Chen et al. carried out a two-step deposition starting with a thermally evaporated CsBr film followed by annealing at 200℃ in $TiBr_4$ vapor at ambient pressure for up to 24 hours to prepare Cs_2TiBr_6 thin films (Figure 5C).[91] In this method, a washing step in toluene was used to remove possible $TiBr_4$ excess at the surface. The Cs_2TiBr_6 films exhibited balanced photogenerated carrier-diffusion lengths of ~ 121 nm and ~ 103 nm for electrons and holes, respectively. The solar cell devices based on the Cs_2TiBr_6 thin films reached a PCE of up to 3.3% while the devices exhibit high stability under heat, moisture, and light.

Igbari et al. carried out a comparison between $Cs_2AgBiBr_6$ films prepared via evaporation deposition (similar to the process shown in Figure 5A) and solution deposition with precursors made from $Cs_2AgBiBr_6$ crystals (Figure 4A) at optimized annealing temperatures of 220 ℃ and 280 ℃, respectively.[115] Grazing incidence X-ray diffraction (GIXRD) and Atomic Force Microscope (AFM) results look similar (Figure 6), including similar domain grain sizes of 206 and 232 nm, at optimized annealing conditions for vapor and solution deposited films, respectively. Photovoltaic devices from solution deposited films however, showed a higher PCE (2.5 versus 1.4 %). It was mentioned that evaporated films suffered from a larger loss of Br, resulting in a deviation from the theoretical 2:1:1:6 ratio of Cs:Ag:Bi:Br. A stoichiometric ratio of Br is necessary where Br^- octahedrally coordinates with Ag^+ to form a high quality and stable compound.[115]

2.2.3 Post deposition annealing

A post annealing process is an essential step involved in most if not all reported synthesis routes for halide double perovskites. Especially for solution-based routes, the post-annealing step is important because it removes the residual solvent and other volatile components.[9] In addition, the annealing process promotes the conversion of the precursor and precursor phases into the desired phase-pure double perovskite.[94] On the other hand, the morphology and the crystallinity of the as-deposited film can be optimized by the annealing process triggering grain growth and coarsening.

Gao et al. investigated the effect of annealing temperature on morphology and crystallinity of $Cs_2AgBiBr_6$ thin films synthesized by antisolvent-assisted solution deposition.[100] An increase in crystallinity with increasing post-annealing temperature was found accompanied by a gradual increase of grain size from ~38 nm in as-deposited films up to an average ~410 nm when annealed at 300°C. Igbari et al.

compared the effect of the annealing temperature on the crystallinity of $Cs_2AgBiBr_6$ thin films synthesized by solution versus vacuum processing.[115] In this work, vacuum processing was performed by five deposition cycles of CsBr/AgBr/BiBr3 stacks, each with a 2:1:1 molar ratio. The XRD patterns show that the highest diffraction peak intensities were obtained at annealing temperatures of 280 °C for 5 min versus 220 °C for 30 min for thin films synthesized by solution versus vacuum processing, respectively. The temperature difference was attributed to the nature of the as-deposited films. For the vacuum deposited film, the stacking sequence of halide films was suspected to facilitate thermal interdiffusion reactions required to form a phase pure $Cs_2AgBiBr_6$ film. While for the solution deposited films, higher film quality requires a fast removal of the residual solvent,[95,115,123,124] thus, a higher annealing temperature combined with short annealing time is beneficial. The solution-processed $Cs_2AgBiBr_6$ films exhibited higher crystallinity, smaller bandgap, longer photoexcitation lifetime, and higher mobility, resulting in a PCE of 2.5% (in comparison to 1.4% for the vacuum-deposited films). These superior properties were attributed to a better film stoichiometry.

The post-deposition annealing time reported for halide double perovskite thin films synthesized via solution deposition is typically in the minutes range.[41,94–97,99,100,102–104,107,115] This annealing time is shorter than required for vapor deposited films from elemental precursors, which is typically varied from minutes up to several hours[87,115,125]. Possibly, the latter requires longer annealing times to ensure a complete nanoscale solid state reaction of the precursors.[115] For example, Wang et al. optimized a two-step annealing process on sequential-vapor-deposited $Cs_2AgBiBr_6$ thin films, in which the as-deposited films were annealed at each temperature for 5 h (200 °C first, then 240 °C).[87]

In general, the maximum annealing temperatures that hybrid ABX_3 and all-inorganic perovskites can tolerate are ~150-160 °C and ~300 °C, respectively.[9] The hybrid organic-inorganic ABX_3 perovskites are prone to decomposition at higher temperatures. Although most ABX_3 perovskites require an annealing step there exist room-temperature additive-assisted synthesis routes demonstrating high solar conversion efficiency (> 18 %) and improved current-voltage hysteresis.[126] Room-temperature processing can be beneficial in limiting interlayer reactions with adjacent layers in a device configuration, and when it comes to upscaling and high throughput. Another strategy to enhance crystallinity and grain size is via a so called "solvent annealing" as demonstrated for hybrid $MAPbI_3$ and all-inorganic $CsPbX_3$.[127,128] In the process reported by Xiao et al. stacked PbI_2 and MAI were annealed at 100 °C for 1 hour with and without DMF vapor.[127] Grain growth was promoted by enhanced precursor ion and molecule diffusion if exposed to DMF vapor. The application of these methods is yet to be explored in the double perovskite field.

3. Modifications in solution deposition

Thin film quality, including crystallinity, grain size, presence of impurity phases, and defects, can affect the optoelectronic properties to a great extent. This section focuses on how modifications of the solution deposition route influence the resulting properties of halide double perovskite films.

3.1 Preheating

Greul et al. carried out a "preheating step" (also called hot-casting) prior to the spin-coating/post annealing, where the substrate and precursor solution were pre-heated to different temperatures including 65 °C, 75 °C, 100 °C, 125 °C, as illustrated in Figure 7A.[94] It was found that the quality and in particular the substrate coverage of the $Cs_2AgBiBr_6$ films was improved leading to an increase in optical absorption. As a consequence, in optimized photovoltaic devices this not only led to a higher short circuit current density but also increased fill factor and open circuit voltage. A PCE close to 2.5% with V_{oc} exceeding 1 V was obtained for devices prepared with pre-heating at 75 °C, while the devices featured a high stability under constant illumination at ambient conditions. Deterioration of devices performance was observed for devices prepared with preheating at higher temperatures (≥100 °C), which was attributed to the formation of large crystals at the top layer of the double perovskites. An increased surface coverage when preheating the substrate and precursor solution was attributed to the faster solvent evaporation. An increase in precursor concentration ($BiBr_3$, AgBr, and CsBr) was not effective due to the limited precursor solubility at ~0.6 M in DMSO. A similar preheating step for the same material was also reported by Hoye et al.[97]

This strategy was employed for both, hybrid and all-inorganic perovskites typically resulting in up to mm-scale grain size and improved performance due to a reduction in bulk defects and increased carrier mobility.[129,130]

3.2 Low-pressure assisted deposition

In a different strategy to circumvent poor sample coverage, Wu et al. fabricated $Cs_2AgBiBr_6$ films by a low-pressure assisted (LPA) solution desposition approach,[95] which was modified from similar methods reported for ABX_3 perovskites.[131–133] As presented in Figure 7B, the $Cs_2AgBiBr_6$ precursor solution was first spin-coated onto the substrate, and then transferred to a low-pressure chamber (20 Pa), followed by an annealing step at 200 ℃.[95] Comparing the LPA film to a film prepared with conventional thermal annealing, the former exhibited a denser and smoother morphology. As a result, the solar cell based on this $Cs_2AgBiBr_6$ film resulted in a PCE of 1.44%. For the synthesis of ABX_3 perovskites the low pressure was explained to triggers rapid crystallization of the perovskite intermediate phase by a fast solvent removal and circumvent spatially inhomogeneous nucleation.[123] It was further explained that post annealing of the wet film at temperatures above its glass transition, results in dewetting and uncontrolled morphologies with large grain size distribution due to the precursors' increased mobility. During the LPA step, dewetting was prevented due to an increase in viscosity as well as glass transition temperature of the wet thin film.[123] Although this explanation was used for the fabrication of ABX_3 perovskites, a similar reasoning probably applies to the study conducted by Wu et al.

3.3 Solvent Engineering

Another modification of the solution deposition process is the application of an antisolvent during the spin coating step often referred to as solvent engineering method. The nature of an antisolvent is its non solubility of the target phase. Consequently, dripping an antisolvent leads to an accelerated crystallization process, induces homogeneous nucleation with high nucleation density, and therefore promotes uniform grain growth.[134–138] The antisolvent process is very successfully used for the preparation of conventional ABX_3 perovskite films.[139,140] The most commonly used antisolvents include toluene,[139] chlorobenzene,[140] and diethyl ether.[141] To enhance surface coverage, film roughness and morphology, Gao et al. deployed IPA as an antisolvent during the spin coating process of $Cs_2AgBiBr_6$ films (Figure 7C) and reported extremely smooth surfaces with root-mean-square (RMS) roughness of <10 nm.[100] Other antisolvents tested including toluene, chlorobenzene, methanol, and ethanol were found to induce fast crystallization and lead to improved film quality but did not lead to pinhole-free films.[100] It has been reported that IPA is a suitable antisolvent for inorganic compounds as it efficiently removes surface states in $Cs_2AgBiBr_6$.[65]

Finally, to increase the grain size and crystallinity or orientation, Yang et al. used a solvent mixture of DMF and DMSO to dissolve $Cs_2AgBiBr_6$ single crystals and fabricate thin films (Figure 7D).[102] The largest grains with size > 1 µm were observed in the $Cs_2AgBiBr_6$ films made with a DMF ratio of 10%. In the absence of DMF, the average grain size was about 250 nm. It is assumed that presence of DMF results in fewer nucleation sites and facilitates the Ostwald ripening during the formation process. $Cs_2AgBiBr_6$ films made with 10% DMF exhibited higher PL intensity and increased lifetime indicating reduced trap densities. A higher ratio of DMF resulted in the formation and co-presence of $Cs_3Bi_2Br_9$ phase. This was explained by a reduced solubility of AgBr in DMF/DMSO mixtures with high DMF content possibly resulting in a change of the original stoichiometric molar precursor ratio and consequently, impurity phase formation. Films prepared with 10% DMF exhibited larger grain sizes, lower trap densities, and longer charge carrier lifetimes, compared to films prepared with pure DMSO. Moreover, the fabricated photodetectors demonstrated superior operational, thermal, and environmental stability of the resulting devices, making $Cs_2AgBiBr_6$ a promising candidate for photodetector applications under harsh conditions. Notably, due to the low solubility of precursors used for double perovskites synthesis, only a limited number of solvents were employed for solvent engineering strategies, compared to Pb-based perovskites.

4. Compositional engineering and dimensional reduction of double perovskites

Application of halide double perovskites as functional layer in optoelectronic devices is to date in its infancy and requires a better understanding of structural formation, photophysical properties, and importantly, tuneability of optoelectronic properties. Given their rich compositional space, compositional engineering methods can be employed to tune and explore their optoelectronic properties such as magnitude and nature of the bandgap. The compositional selection of $A_2B^+B'^{3+}X_6$ compounds can be guided for example by models to predict electronic structure,[142] high-throughput and machine-learning approaches,[50,143] as well as the stability design rule of the perovskite structure. The latter can be expressed via the tolerance factor τ:[144]

$$\tau = \frac{r_X}{r_B} - n_A\left(n_A - \frac{r_A/r_B}{\ln\left(r_A/r_B\right)}\right) \tag{1}$$

where n_A is the oxidation state of the cation A, r_A, r_B, r_X are the ionic radii of ions A, B, X, respectively, with r_B representing the arithmetic mean radius of the B and B' ions, and $r_A > r_B$ by definition. $\tau < 4.18$ indicates perovskite structure.[144] This new tolerance factor shows higher accuracy than the Goldschmidt tolerance factor t in particular for compounds containing halides which are heavier than oxides and fluorides.[144]

The key contributing factors that determine the success of $APbX_3$ perovskites might be related to the high symmetry of the perovskite and the electronic configuration of Pb being $6s^26p^0$.[7,145] Desirably, the double perovskite structure mimics these properties. In this section, we discuss cation and halide substitution in double perovskites starting briefly with powders and crystals followed by elemental substitutions in thin films and finally, dimensional reduction of double perovskites. This part will not contain detailed implications on defect physics nor details on electronic states and band structure which can be found in recent reviews on this subject matter such as in references.[49,54,56]

Compositional engineering in the broader context of the successful hybrid ABX_3 perovskites, has drawn enormous research interest and is well summarized by Dunlap-Shohl et al. in Ref. [9]. Especially A-site substitution with alkali metals (e.g. Cs) or addition of alkali iodides (NaI, KI) to the precursor solution do not only influence grain growth but also improve PCE, lifetime, and photoluminescence quantum yield. Addition of K during synthesis of $CsPbI_2Br$ led to similar improvements. In general, the beneficial presence of alkali metals was linked to defect passivation. Br substitution on the X-site in hybrid ABX_3 perovskites leads to wider bandgaps with increasing Br content. It was also reported to enhance moisture tolerance but, on the downside, addition of Br between 20-60% leads to light induced halide segregation which can limit performance and in particular the open circuit voltage.

4.1 B^+- and B'^{3+}-site substitution

The choice of the cations at the B^+ and B'^{3+} sites in $A_2B^+B'^{3+}X_6$ has attracted attention because it can tune the bandgap size, shift the electronic bands to form direct bandgap materials, and increase the carrier lifetime.[63,85,110,146–148] It is emphasized that it is generally not straight forward in semiconductors to independently tune the valence and conduction bands. It is however possible in the $A_2B^+B'^{3+}X_6$ structure because one B can form the valence band via d^{10} states while the other B forms the conduction band via s/p states.[62]

With an emphasis on synthesis, the majority of cation substitutions in double perovskites had been performed on crystals and not thin films (Figure 2B). For example, Du et al. substituted part of Bi^{3+} with Sb^{3+} to form $Cs_2Ag(Bi_{1-x}Sb_x)Br_6$ via solid state powder synthesis using mixtures of CsBr, AgBr, $BiBr_3$ and $SbBr_3$ as starting materials.[63] A smallest bandgap of 1.86 eV was obtained for x = 0.375 as compared to 2.12 eV for x = 0. Interestingly, Slavney et al. synthesized $Cs_2AgTlCl_6$ and $Cs_2AgTlBr_6$ powders using solution processing and found direct bandgaps that are ~1 eV smaller as compared to their halide analogues Cs_2AgBiX_6.[146] It should be noted that Tl is much more toxic than Pb but it provides mechanistic insights into the tuneability of optoelectronic properties of double perovskites. Similarly, Tran et al. demonstrated that a transition from an indirect ($Cs_2AgSbCl_6$) to a direct bandgap ($Cs_2AgInCl_6$) is possible in $Cs_2AgSb_xIn_{1-x}Cl_6$ for x = 0.4 synthesized via solid state reaction in sealed quartz ampoules.[62] Using hydrothermal synthesis for a vacancy-ordered double perovskite $A_2B^{4+}X_6$, Tan et al. prepared Bi-doped Cs_2SnCl_6 by adding $BiCl_3$ to the precursor and obtained a significantly reduced bandgap of 3 eV as compared to 3.9 eV of the undoped material.[86] The smaller bandgap was attributed to defect bands created by the Bi^{3+} dopant which boosted the photoluminescence quantum yield from < 1% to 78.9%.

Turning our attention now to thin films, Liu et al. demonstrated bandgap engineering of $Cs_2AgSb_xBi_{1-x}Br_6$ by replacing up to 75% of Bi with Sb.[110] The synthesis route follows a solution-based method under Ar atmosphere, and the precursor was prepared by mixing CsBr, AgBr, $SbBr_3$, and $BiBr_3$ powders in a ratio of 2:1:x:(1-x) in DMSO solution. Subsequently, phase pure $Cs_2AgSb_xBi_{1-x}Br_6$ films were obtained from dip coating followed by a post-annealing process. The optical appearance of the thin films exhibits a gradual color shift from yellow-orange to red as the portion of Sb is increased from 0 to 0.75 (Figure 8A), which is in agreement with the transmittance spectra and corresponding to a decrease in bandgap from 2.22 to 1.97 eV (Figure 8B). The microstructures shown in Figure 8C revealed that Bi-rich samples (left-hand side) exhibit a higher crystal quality than the Sb-rich ones (right-hand side). Comparing with reference $Cs_2AgBiBr_6$ film, the average PCE of the fabricated solar cell devices with $Cs_2AgSb_{0.25}Bi_{0.75}Br_6$ film increased from 0.19% to 0.25% but decreased significantly with more Sb. Additionally, the authors noted that it was impossible to obtain phase pure $Cs_2AgSbBr_6$ films with 100% Sb as had been found previously by Mitzi and co-workers using a solid state sintering method.[63]

Luo et al. synthesized Bi-doped and Na-alloyed $Cs_2Ag_xNa_{1-x}InCl_6$ crystals and thin films via hydrothermal synthesis and sequential thermal evaporation ($CsCl/InCl_3/BiCl_3/NaCl/AgCl$) followed by annealing at 150℃ in N_2 for 5 min, respectively.[82] A drastic increase in photoluminescence quantum yield by three orders of magnitude was found when alloying $Cs_2AgInCl_6$ with Na cations which was attributed to the breaking of the dark (parity-forbidden) transition. In addition to Na alloying of $Cs_2Ag_xNa_{1-x}InCl_6$, doping with Bi provides a passivation for the deep defects caused by In^{3+}, which enhances crystal perfection and thus reduces the sub-bandgap absorption (Figure 9A) and increases photoluminescence lifetime (Figure 9B). Both, incorporation of Bi plus slow cooling yielded a highest quantum yield of 86±5% (Figure 9C). Both Bi doping and Na alloying have allowed highly efficient and stable warm-white light emission which can be used for next-generation lighting and display technologies.

4.2 X-site substitution

Although a widely adapted strategy in the ABX_3 perovskite community,[149,150] halide substitution has not been deployed extensively for halide double perovskites. For example, according to computational research, variation of X in Cs_2AgBiX_6 can alter the bandgap from 2.7 eV > 2.3 eV > 1.6 eV for X = Cl, Br, I, respectively.[41] Cs_2AgBiI_6

however, is not thermodynamically stable[121] with even small amounts of iodine incorporation resulting in the formation of low dimensional $Cs_3Bi_2I_9$ phase.[83,151,152] As an alternative, the sulphide anion can induce a bandgap reduction by upshifting the valence band which was demonstrated in the silver bismuth sulfoiodide material with formula $Ag_aBi_bI_{a+3b-2x}S_x$.[153] Inspired by this, Pai et al. fabricated $Cs_2AgBiBr_{6-2x}S_x$ thin films by substitution of Br with S via sulphide modification.[108] The synthesis strategy follows a typical solution-based route as discussed below in section 2.2.1 (Figure 4A), in which the DMSO-based precursor was modified by adding bismuth(III) tris(4-methylbenzothiolate) ($Bi(S_2CAr)_3$). During the post-annealing step at 280 ℃, $Bi(S_2CAr)_3$ decomposes to S^{2-} and volatile co-products to form $Cs_2AgBiBr_{6-2x}S_x$. Small amounts of sulfur ($x \leq 0.1$) incorporation retained the pinhole free, homogeneous morphology (Figure 10A). The introduction of higher amounts of sulfur ($x \geq 0.2$) induced significant deterioration of the morphology as revealed by the presence of a substantial amount of pin-holes and poorly conducting impurities on the surface of the films (Figure 10A). With $x \leq 0.2$, minor XRD peak shifts were observed but the cubic crystal geometry was preserved while larger fraction of S^{2-} led to emergence of new diffraction peaks from impurity phases. A slight bandgap reduction from 2.37 eV (for $Cs_2AgBiBr_6$) to 2.30 eV (for $Cs_2AgBiBr_{5.7}S_{0.15}$) was found due to a valence band upwards shift (Figure 10B). Due to the notable enhancements in the intrinsic light absorption with the introduction of sulfur, improvements by up to 50% in the photocurrent density were obtained from the corresponding thin-film solar cells. These enhancements have resulted in improved PCE of ~1.9% for solar cells based on $Cs_2AgBiBr_{5.8}S_{0.1}$, compared to PCE of ~1.3% for the unmodified $Cs_2AgBiBr_6$. Moreover, the solar cell devices based on $Cs_2AgBiBr_{5.8}S_{0.1}$ demonstrated excellent stability against all common environmental stimuli, including heat, light, and humidity.

By both, first-principle computations and experimental measurements on synthesized bulk material using the melt crystallization process, Ju et al. demonstrated that the bandgap of the mixed-halide double perovskite $Cs_2TiI_{6-x}Br_x$ can be tailored from 1.02 to 1.78 eV.[40] In particular, $Cs_2TiI_2Br_4$ exhibits a bandgap of 1.38 eV, which is ideal for application in single-junction PSC. Lee et al. synthesized $Cs_2SbI_{6-x}Br_x$ thin films by a two-step solution synthesis method with starting binary precursors including CsI, CsBr, SnI_4, and $SnBr_4$.[112] Solutions of Sn-halide were reacted with electro-sprayed Cs-halide films followed by air annealing at 110℃ for 20 min. The reaction was described as follows:

$$(1\text{-}x)CsI + xCsBr + SnX_4\ (X = I, Br) \rightarrow Cs_2SnI_{6\text{-}x}Br_x$$

With increasing Br, the diffraction peaks are shifting towards higher diffraction angles (Figure 10D). Visual appearance of the thin films changes from dark brown to light yellow when substituting I with Br in accordance with a gradual bandgap increase from 1.3 to 2.9 eV (Figure 10E). The fabricated solar cell devices based on the mixed halides $Cs_2SnI_4Br_2$ exhibited not only improved performance (with PCE ~ 2%) compared to Cs_2SnI_4 (with PCE ~ 1.5%) but also higher stability in air. This behavior of solar cell performance was attributed to the compromise of decreased short-circuit current (J_{sc}) and increased open-circuit voltage (V_{oc}) with increasing Br content, corresponding to decreased absorption and increased energy gap, respectively. The subset of examples discussed above illustrate many variations of substitutional modifications at cation and anion sites to not only tune but also optimize optoelectronic properties of lead-free double perovskites.

4.3 Dimensional reduction of double perovskites

While the 3D double perovskites offer considerable opportunities for compositional design, the expansion to lower-dimensional double perovskites can further enhance tunability of optoelectronic properties. For instance, reducing the dimensionality of double perovskites can be used as a strategy to tailor direct bandgap materials (see Figure 11A).[51] Moreover, 2D double perovskite films offer the opportunity to create strong anisotropy along in-plane and out-of-plane directions (Figure 11B) which can be used for novel electronic and optoelectronic applications.[154] The 2D derivatives of hybrid double perovskites can be formed when the A site is occupied by too large organic cations.[155] In this case, the structural design rules are not limited by the tolerance factor making the 2D double perovskite structure more flexible. Through the choice of cation spacers, two distinct types of hybrid 2D layered double perovskites can be obtained, including the Ruddlesden–Popper (RP) and the Dion–Jacobson (DJ) structures.[155]

The deposition of layered 2D double perovskite thin films commonly relies on preparing solutions by dissolving pre-synthesized crystals in DMSO or DMF followed by spin coating and thermal annealing procedure.[51,156,157] These crystals are mostly fabricated by hydrothermal synthesis based on precursors containing metal bromides or metal oxides (or a mixture of both) combined with an organic compound (i.e., spacer).[51,155,158–161] By replacing Cs with the organic ligand BA (BA = $CH_3(CH_2)_3NH_3^+$) in $Cs_2AgBiBr_6$, Connor et al. synthesized the 2D single crystal analogues $(BA)_4AgBiBr_8$ (n=1) and $(BA)_2CsAgBiBr_7$ (n=2).[51] The former exhibit a direct bandgap, whereas the latter showed an indirect bandgap similar to the 3D double perovskite $Cs_2AgBiBr_6$ ($n=\infty$). $(BA)_4AgBiBr_8$ single crystals were made by hydrothermal synthesis where mixtures of butylamine ($CH_3(CH_2)_3NH_2$) and metal bromides (AgBr and $BiBr_3$) were dissolved in concentrated HBr at 100°C, then slowly cooled to room temperature to form flat rectangular crystals. The according thin films were then prepared by spin coating dissolved crystals in DMF followed by air annealing at 100 °C for 4 minutes. The layered 2D $(BA)_4AgBiBr_8$ has been shown to exhibit pressure-induced emission (Figure 11C) and change in bandgap as a function of pressure, making the material a potential candidate for applications in the fields of pressure sensing and information storage.[158]

Large-size plate-like crystals of $(BA)_2CsAgBiBr_7$ (with size up to $10\times10\times3$ mm^3) were obtained by dissolving stoichiometric quantities of Ag_2O (1.5 mmol), Bi_2O_3 (1.5 mmol), and Cs_2CO_3 (1.5 mmol) with 10 equivalents of butylamine (15 mmol) in HBr solution at 373 K.[159] The solution was slowly cooled at a rate of 0.5 K /day in a closed heating oven where the large-size crystals were harvested after several days. The harvested crystals were cleaned and dried in a N_2-filled glovebox overnight, and then heated at 70 °C for 2 h to release lattice stress and remove moisture. This material has shown large mobility-lifetime product, high bulk resistivity, low density of defects and traps, and strong X-ray attenuation, offering the opportunity for efficient X-ray detection. Novel ferroelectric 2D double perovskites based on $(CPA)_4AgBiBr_8$ (CPA=chloropropylammonium) were synthesized using hydrothermal method, and show X-ray sensitivity (Figure 11D).[161]

As a last example, thin films of $(NH_3C_6H_{10}NH_3^{+2})_2AgBiI_8\cdot H_2O$ and $(C_6H_{16}N_2)_2CuBiI_8\cdot 0.5H_2O$ with $NH_2C_6H_{10}NH_2$ = 1,4-cyclohexanediamine were fabricated through spin-coating solutions of their pre-synthesized crystals in DMF, followed by annealing in air at 70 °C.[156] The films exhibited optical band gaps of 1.93 and 1.68 eV, respectively, and both showed obvious photoconductivity under illumination, see Figure 11E. Furthermore, both materials exhibited high stability against moisture and heat when either stored at 55% relative humidity for 30 days or heated at 100 °C in air for 72 h. Notably, the annealing for 2D hybrid organic-inorganic double perovskites is often performed at relatively lower temperatures as compared to all-inorganic 3D double perovskites. To conclude, through the selection of organic spacing cations, the halide, and metal alloying, these low dimensional compounds have shown structural diversity and tunable optoelectronic properties.[155]

5. Conclusions and Outlook

Thermally more stable all-inorganic perovskites, $CsPb(I,Br)_3$, are a promising perovskite sub-field which can be used here to discuss similarities and differences with halide double perovskites. In both cases, solution processing methods are complicated due to the challenges related to the limited solubility of Cs halides. Both, vapor deposition methods and sequential solution deposition can help to manage solubility challenges. As an example, large grained $CsPbBr_3$ films were obtained by spin-casting $PbBr_2$ followed by dipping in a heated CsBr solution.[163] Taking inspiration from the ABX_3 perovskite field, there are many synthetic variations yet to be applied to double perovskites to manipulate and control film growth. These include two step deposition approaches, use of antisolvents, additives, post-treatments, solvent engineering, non-stoichiometric precursor ratios, and non-halide 'spectator' precursors.[9] Further research efforts are required to systematically investigate the role of these variables on crystallization pathways and kinetics. As an example, *in situ* synchrotron diffraction measurements can provide valuable insights and unveil precursor transformation kinetics and secondary phase evolution.[164] The independent control of nucleation and growth during processing of ABX_3 perovskites was identified as a major step towards high quality films including fast initial nucleation to promote uniform coverage but omit microstructural defects.[9] In-depth studies are needed to deconvolve these processes and provide a mechanistic understanding of how nucleation can be promoted and controlled. Possibly, *in situ* microscopy or PL[138] can provide viable means for such investigations.

Moreover, defect passivation strategies are indispensable to limit detrimental non-radiative recombination, ion migration, charge trapping, and current density-voltage hysteresis.[165] A recent study on $Cs_2AgBiBr_6$ and $Cs_2AgTlBr_6$ single crystals found very high surface trap densities which were likely linked to halogen degassing.[53] Possibly, as successfully demonstrated for all-inorganic perovskites, film growth under CsBr-rich versus equimolar solutions can be beneficial and reduce surface trap states.[166] Several defect passivation strategies proved to be very effective in boosting the open-circuit voltage and therefore enhanced the radiative recombination in inorganic perovskites. For example, Mn^{2+} doping in $CsPbI_2Br$ was found to retard the growth rate enabling micro-crystalline films and at the same time passivated defects along grain boundaries and at the surface.[167] By adding a small amount of $CaCl_2$ to the precursor solution a record open circuit voltage of 1.32 V has been demonstrated recently for $CsPbI_2Br$ solar cells with improved crystallinity and reduced trap density.[168] Dedicated efforts to develop defect passivation strategies in double perovskites are still lacking but can provide a very promising route to control film quality and enhance device performance.

This review was inspired by a text mining effort that summarized the halide double perovskite field based on deployed synthesis techniques and differentiated by their elemental composition. The number of halide double perovskite compounds experimentally realized lags far behind the increasing number of stable compositions with suitable optoelectronic properties that are theoretically predicted. In comparison with ABX_3 perovskites, research and optimization of synthetic approaches is still in its infancy including the fabrication of high quality functional thin films. A large portion of the review was dedicated to $Cs_2AgBiBr_6$ since this is the most investigated representative halide double perovskite. Both, vapor deposition and solution-based methods have been successfully used for the preparation of thin films of different halide double perovskite compositions. The reported properties for the same composition such as phase purity, bandgap and PL lifetime, however, vary with synthesis method. Generally, the processing temperatures for double perovskite thin films are varied and mostly > 200 °C i.e. higher than typical processing temperatures employed for the synthesis of ABX_3 perovskites (~100-150 °C), but still comparatively low or moderate if contrasted with chalcogenides (e.g. CIGS, CdTe) or traditional III-Vs (GaAs, InP).

Besides higher stability towards heat, moisture, oxygen, and light, as compared to $CH_3NH_3PbI_3$ (with highly hygroscopic MA^+) halide double perovskites feature independent tunability of valence and conduction band. In this regard, quaternary halide double perovskites have high compositional dimensionality which can be exploited by A, B/B', and X-site alloying. Especially, given the fact that ABX_3 perovskites show better performance and stability with higher elemental complexity,[169] the research field of substitutional modifications of double halide perovskite compositions presents a future avenue to be explored. Dimensional reduction of the 3D $A_2BB'X_6$ structure might provide another layer of control for the rational design of emergent halide double perovskites.[159] Ultimately, a combination of perfectly finetuned chemistry and synthetic approach that can yield a superior halide double perovskite material yet needs to be demonstrated. Given this potential we expect the field to grow continually in the future but compared to ABX_3 perovskites it still lacks successful device implementation beyond rather scattered proof of concept studies which might inhibit exponential growth of this field. As a next step, computational and high throughput synthesis efforts need to reduce the $>10^6$ possible Pb-free perovskite combinations to a few, maybe hundred, that are predicted to resemble the outstanding optoelectronic properties of ABX_3. This effort should be closely connected to tailoring the synthesis methods and application of dedicated defect passivation strategies to produce high quality thin films.

Acknowledgements

This work was funded by the U.S. Department of Energy, Office of Science, Office of Basic Energy Sciences, Materials Sciences and Engineering Division under Contract No. DE-AC02-05-CH11231 (D2S2 program KCD2S2). Support from the Molecular Foundry supported by the Office of Science, Office of Basic Energy Sciences, of the U.S. Department of Energy under Contract No. DE-AC02-05CH11231 is acknowledged.

Author contribution

Y.Z., M.A., and C.M.S.-F. have conceptualized and written the paper. K.C. and G.C. have extracted synthesis details from existing literature. All authors have given final approval to the review paper.

Conflict of Interest

The authors declare no conflict of interest.

Keywords

Halide double perovskite, synthesis, thin film, Pb-free

Corresponding Author

csutterfella@lbl.gov

Reference

1. Kojima, A., Teshima, K., Shirai, Y., and Miyasaka, T. (2009). Organometal halide perovskites as visible-light sensitizers for photovoltaic cells. J. Am. Chem. Soc. *131*, 6050–6051.
2. National Renewable Energy Laboratory (2021). Best Research-Cell Efficiency Chart. https://www.nrel.gov/pv/cell-efficiency.html.
3. Grätzel, M. (2014). The light and shade of perovskite solar cells. Nat. Mater. *13*, 838–842.
4. Green, M.A., Ho-Baillie, A., and Snaith, H.J. (2014). The emergence of perovskite solar cells. Nat. Photonics *8*, 506–514.
5. Herz, L.M. (2016). Charge-Carrier Dynamics in Organic-Inorganic Metal Halide Perovskites. Annu. Rev. Phys. Chem. *67*, 65–89.
6. Stranks, S.D., Eperon, G.E., Grancini, G., Menelaou, C., Alcocer, M.J.P., Leijtens, T., Herz, L.M., Petrozza, A., and Snaith, H.J. (2013). Electron-Hole Diffusion Lengths Exceeding Trihalide Perovskite Absorber. Science *342*, 341–344.
7. Yin, W.J., Shi, T., and Yan, Y. (2014). Unique properties of halide perovskites as possible origins of the superior solar cell performance. Adv. Mater. *26*, 4653–4658.
8. Sutter-Fella, C.M., Li, Y., Amani, M., Ager, J.W., Toma, F.M., Yablonovitch, E., Sharp, I.D., and Javey, A. (2016). High Photoluminescence Quantum Yield in Band Gap Tunable Bromide Containing Mixed Halide Perovskites. Nano Lett. *16*, 800–806.
9. Dunlap-Shohl, W.A., Zhou, Y., Padture, N.P., and Mitzi, D.B. (2019). Synthetic Approaches for Halide Perovskite Thin Films. Chem. Phys. *119*, 3193–3295.
10. Jung, Y.S., Hwang, K., Heo, Y.J., Kim, J.E., Vak, D., and Kim, D.Y. (2018). Progress in Scalable Coating and Roll-to-Roll Compatible Printing Processes of Perovskite Solar Cells toward Realization of Commercialization. Adv. Opt. Mater. *6*, 1–30.
11. Jeon, N.J., Noh, J.H., Yang, W.S., Kim, Y.C., Ryu, S., Seo, J., and Seok, S. Il (2015). Compositional engineering of perovskite materials for high-performance solar cells. Nature *517*, 476–480.
12. McMeekin, D.P., Sadoughi, G., Rehman, W., Eperon, G.E., Saliba, M., Hörantner, M.T., Haghighirad, A., Sakai, N., Korte, L., Rech, B., et al. (2016). A mixed-cation lead mixed-halide perovskite absorber for tandem solar cells. Science *351*, 151–155.
13. Saliba, M., Matsui, T., Seo, J.Y., Domanski, K., Correa-Baena, J.P., Nazeeruddin, M.K., Zakeeruddin, S.M., Tress, W., Abate, A., Hagfeldt, A., et al. (2016). Cesium-containing triple cation perovskite solar cells: Improved stability, reproducibility and high efficiency. Energy Environ. Sci. *9*, 1989–1997.
14. Hong, K., Le, Q. Van, Kim, S.Y., and Jang, H.W. (2018). Low-dimensional halide

perovskites: Review and issues. J. Mater. Chem. C *6*, 2189–2209.

15. Hoefler, S.F., Trimmel, G., and Rath, T. (2017). Progress on lead-free metal halide perovskites for photovoltaic applications: a review. Monatshefte fur Chemie *148*, 795–826.
16. Dong, Q., Liu, F., Wong, M.K., Tam, H.W., Djurišić, A.B., Ng, A., Surya, C., Chan, W.K., and Ng, A.M.C. (2016). Encapsulation of Perovskite Solar Cells for High Humidity Conditions. ChemSusChem *9*, 2597–2603.
17. Abate, A. (2017). Perovskite Solar Cells Go Lead Free. Joule *1*, 659–664.
18. Yang, D., Lv, J., Zhao, X., Xu, Q., Fu, Y., Zhan, Y., Zunger, A., and Zhang, L. (2017). Functionality-Directed Screening of Pb-Free Hybrid Organic-Inorganic Perovskites with Desired Intrinsic Photovoltaic Functionalities. Chem. Mater. *29*, 524–538.
19. Kopacic, I., Friesenbichler, B., Hoefler, S.F., Kunert, B., Plank, H., Rath, T., and Trimmel, G. (2018). Enhanced Performance of Germanium Halide Perovskite Solar Cells through Compositional Engineering. ACS Appl. Energy Mater. *1*, 343–347.
20. Hao, F., Stoumpos, C.C., Cao, D.H., Chang, R.P.H., and Kanatzidis, M.G. (2014). Lead-free solid-state organic-inorganic halide perovskite solar cells. Nat. Photonics *8*, 489–494.
21. Stoumpos, C.C., Frazer, L., Clark, D.J., Kim, Y.S., Rhim, S.H., Freeman, A.J., Ketterson, J.B., Jang, J.I., and Kanatzidis, M.G. (2015). Hybrid germanium iodide perovskite semiconductors: Active lone pairs, structural distortions, direct and indirect energy gaps, and strong nonlinear optical properties. J. Am. Chem. Soc. *137*, 6804–6819.
22. Wang, F., Ma, J., Xie, F., Li, L., Chen, J., Fan, J., and Zhao, N. (2016). Organic Cation-Dependent Degradation Mechanism of Organotin Halide Perovskites. Adv. Funct. Mater. *26*, 3417–3423.
23. Wang, N., Zhou, Y., Ju, M.G., Garces, H.F., Ding, T., Pang, S., Zeng, X.C., Padture, N.P., and Sun, X.W. (2016). Heterojunction-Depleted Lead-Free Perovskite Solar Cells with Coarse-Grained B-γ-$CsSnI_3$ Thin Films. Adv. Energy Mater. *6*, 1–10.
24. Song, T. Bin, Yokoyama, T., Stoumpos, C.C., Logsdon, J., Cao, D.H., Wasielewski, M.R., Aramaki, S., and Kanatzidis, M.G. (2017). Importance of reducing vapor atmosphere in the fabrication of Tin-based perovskite solar cells. J. Am. Chem. Soc. *139*, 836–842.
25. Klug, M.T., Osherov, A., Haghighirad, A.A., Stranks, S.D., Brown, P.R., Bai, S., Wang, J.T.W., Dang, X., Bulović, V., Snaith, H.J., et al. (2017). Tailoring metal halide perovskites through metal substitution: Influence on photovoltaic and material properties. Energy Environ. Sci. *10*, 236–246.
26. Shao, S., Liu, J., Portale, G., Fang, H.H., Blake, G.R., ten Brink, G.H., Koster, L.J.A., and Loi, M.A. (2018). Highly Reproducible Sn-Based Hybrid Perovskite Solar Cells with 9% Efficiency. Adv. Energy Mater. *8*.
27. Liao, W., Zhao, D., Yu, Y., Grice, C.R., Wang, C., Cimaroli, A.J., Schulz, P., Meng, W., Zhu, K., Xiong, R.G., et al. (2016). Lead-Free Inverted Planar Formamidinium Tin Triiodide Perovskite Solar Cells Achieving Power Conversion Efficiencies up to 6.22%. Adv. Mater. *28*, 9333–9340.
28. Giustino, F., and Snaith, H.J. (2016). Toward Lead-Free Perovskite Solar Cells. ACS Energy Lett. *1*, 1233–1240.
29. Lehner, A.J., Fabini, D.H., Evans, H.A., Hébert, C.A., Smock, S.R., Hu, J., Wang, H., Zwanziger, J.W., Chabinyc, M.L., and Seshadri, R. (2015). Crystal and Electronic

Structures of Complex Bismuth Iodides $A_3Bi_2I_9$ (A = K, Rb, Cs) Related to Perovskite: Aiding the Rational Design of Photovoltaics. Chem. Mater. *27*, 7137–7148.

30. Jiang, F., Yang, D., Jiang, Y., Liu, T., Zhao, X., Ming, Y., Luo, B., Qin, F., Fan, J., Han, H., et al. (2018). Chlorine-Incorporation-Induced Formation of the Layered Phase for Antimony-Based Lead-Free Perovskite Solar Cells. J. Am. Chem. Soc. *140*, 1019–1027.

31. Ran, C., Wu, Z., Xi, J., Yuan, F., Dong, H., Lei, T., He, X., and Hou, X. (2017). Construction of Compact Methylammonium Bismuth Iodide Film Promoting Lead-Free Inverted Planar Heterojunction Organohalide Solar Cells with Open-Circuit Voltage over 0.8 V. J. Phys. Chem. Lett. *8*, 394–400.

32. Abulikemu, M., Ould-Chikh, S., Miao, X., Alarousu, E., Murali, B., Ngongang Ndjawa, G.O., Barbé, J., El Labban, A., Amassian, A., and Del Gobbo, S. (2016). Optoelectronic and photovoltaic properties of the air-stable organohalide semiconductor $(CH_3NH_3)_3Bi_2I_9$. J. Mater. Chem. A *4*, 12504–12515.

33. Park, B.W., Philippe, B., Zhang, X., Rensmo, H., Boschloo, G., and Johansson, E.M.J. (2015). Bismuth Based Hybrid Perovskites $A_3Bi_2I_9$ (A: Methylammonium or Cesium) for Solar Cell Application. Adv. Mater. *27*, 6806–6813.

34. Zhang, Z., Li, X., Xia, X., Wang, Z., Huang, Z., Lei, B., and Gao, Y. (2017). High-Quality $(CH_3NH_3)_3Bi_2I_9$ Film-Based Solar Cells: Pushing Efficiency up to 1.64%. J. Phys. Chem. Lett. *8*, 4300–4307.

35. Saparov, B., Hong, F., Sun, J.P., Duan, H.S., Meng, W., Cameron, S., Hill, I.G., Yan, Y., and Mitzi, D.B. (2015). Thin-Film Preparation and Characterization of $Cs_3Sb_2I_9$: A Lead-Free Layered Perovskite Semiconductor. Chem. Mater. *27*, 5622–5632.

36. Harikesh, P.C., Mulmudi, H.K., Ghosh, B., Goh, T.W., Teng, Y.T., Thirumal, K., Lockrey, M., Weber, K., Koh, T.M., Li, S., et al. (2016). Rb as an Alternative Cation for Templating Inorganic Lead-Free Perovskites for Solution Processed Photovoltaics. Chem. Mater. *28*, 7496–7504.

37. Hebig, J.C., Kühn, I., Flohre, J., and Kirchartz, T. (2016). Optoelectronic Properties of $(CH_3NH_3)_3Sb_2I_9$ Thin Films for Photovoltaic Applications. ACS Energy Lett. *1*, 309–314.

38. Zuo, C., and Ding, L. (2017). Lead-free Perovskite Materials $(NH_4)_3Sb_2I_xBr_{9-x}$. Angew. Chemie - Int. Ed. *56*, 6528–6532.

39. Lee, B., Stoumpos, C.C., Zhou, N., Hao, F., Malliakas, C., Yeh, C.Y., Marks, T.J., Kanatzidis, M.G., and Chang, R.P.H. (2014). Air-stable molecular semiconducting iodosalts for solar cell applications: Cs_2SnI_6 as a hole conductor. J. Am. Chem. Soc. *136*, 15379–15385.

40. Ju, M.G., Chen, M., Zhou, Y., Garces, H.F., Dai, J., Ma, L., Padture, N.P., and Zeng, X.C. (2018). Earth-Abundant Nontoxic Titanium(IV)-based Vacancy-Ordered Double Perovskite Halides with Tunable 1.0 to 1.8 eV Bandgaps for Photovoltaic Applications. ACS Energy Lett. *3*, 297–304.

41. Volonakis, G., Filip, M.R., Haghighirad, A.A., Sakai, N., Wenger, B., Snaith, H.J., and Giustino, F. (2016). Lead-Free Halide Double Perovskites via Heterovalent Substitution of Noble Metals. J. Phys. Chem. Lett. *7*, 1254–1259.

42. Volonakis, G., Haghighirad, A.A., Milot, R.L., Sio, W.H., Filip, M.R., Wenger, B., Johnston, M.B., Herz, L.M., Snaith, H.J., and Giustino, F. (2017). $Cs_2InAgCl_6$: A New Lead-Free Halide Double Perovskite with Direct Band Gap. J. Phys. Chem. Lett. *8*, 772–778.

43. Slavney, A.H., Hu, T., Lindenberg, A.M., and Karunadasa, H.I. (2016). A Bismuth-Halide

Double Perovskite with Long Carrier Recombination Lifetime for Photovoltaic Applications. J. Am. Chem. Soc. *138*, 2138–2141.

44. McClure, E.T., Ball, M.R., Windl, W., and Woodward, P.M. (2016). Cs_2AgBiX_6 (X = Br, Cl): New Visible Light Absorbing, Lead-Free Halide Perovskite Semiconductors. Chem. Mater. *28*, 1348–1354.

45. Majher, J.D., Gray, M.B., Strom, T.A., and Woodward, P.M. (2019). $Cs_2NaBiCl_6:Mn^{2+}$ - A New Orange-Red Halide Double Perovskite Phosphor. Chem. Mater. *31*, 1738–1744.

46. Shi, D., Adinolfi, V., Comin, R., Yuan, M., Alarousu, E., Buin, A., Chen, Y., Hoogland, S., Rothenberger, A., Katsiev, K., et al. (2015). Low trap-state density and long carrier diffusion in organolead trihalide perovskite single crystals. Science *347*, 519–522.

47. Zhao, X.G., Yang, J.H., Fu, Y., Yang, D., Xu, Q., Yu, L., Wei, S.H., and Zhang, L. (2017). Design of Lead-Free Inorganic Halide Perovskites for Solar Cells via Cation-Transmutation. J. Am. Chem. Soc. *139*, 2630–2638.

48. Zhao, X.G., Yang, D., Sun, Y., Li, T., Zhang, L., Yu, L., and Zunger, A. (2017). Cu-In Halide Perovskite Solar Absorbers. J. Am. Chem. Soc. *139*, 6718–6725.

49. Igbari, F., Wang, Z.K., and Liao, L.S. (2019). Progress of Lead-Free Halide Double Perovskites. Adv. Energy Mater. *9*, 1–32.

50. Chakraborty, S., Xie, W., Mathews, N., Sherburne, M., Ahuja, R., Asta, M., and Mhaisalkar, S.G. (2017). Rational Design: A High-Throughput Computational Screening and Experimental Validation Methodology for Lead-Free and Emergent Hybrid Perovskites. ACS Energy Lett. *2*, 837–845.

51. Connor, B.A., Leppert, L., Smith, M.D., Neaton, J.B., and Karunadasa, H.I. (2018). Layered halide double perovskites: Dimensional reduction of $Cs_2AgBiBr_6$. J. Am. Chem. Soc. *140*, 5235–5240.

52. Bartesaghi, D., Slavney, A.H., Gélvez-Rueda, M.C., Connor, B.A., Grozema, F.C., Karunadasa, H.I., and Savenije, T.J. (2018). Charge Carrier Dynamics in $Cs_2AgBiBr_6$ Double Perovskite. J. Phys. Chem. C *122*, 4809–4816.

53. Delor, M., Slavney, A.H., Wolf, N.R., Filip, M.R., Neaton, J.B., Karunadasa, H.I., and Ginsberg, N.S. (2020). Carrier Diffusion Lengths Exceeding 1 μm despite TraLimited Transport in Halide Double Perovskites. ACS Energy Lett. *5*, 1337–1345.

54. Zhao, X., Yang, D., Ren, J., Sun, Y., Xiao, Z., and Zhang, L. (2018). Rational Design of Halide Double Perovskites for Optoelectronic Applications. Joule *2*, 1662–1673.

55. Cai, Y., Xie, W., Teng, Y.T., Harikesh, P.C., Ghosh, B., Huck, P., Persson, K.A., Mathews, N., Mhaisalkar, S.G., Sherburne, M., et al. (2019). High-throughput Computational Study of Halide Double Perovskite Inorganic Compounds. Chem. Mater. *31*, 5392–5401.

56. Kung, P.-K., Li, M.-H., Lin, P.-Y., Jhang, J.-Y., Pantaler, M., Lupascu, D.C., Grancini, G., and Chen, P. (2020). Lead-Free Double Perovskites for Perovskite Solar Cells. Sol. RRL *4*, 1900306.

57. Xu, X., Zhong, Y., and Shao, Z. (2019). Double Perovskites in Catalysis, Electrocatalysis, and Photo(electro)catalysis. Trends Chem. *1*, 410–424.

58. Kononova, O., Huo, H., He, T., Rong, Z., Botari, T., Sun, W., Tshitoyan, V., and Ceder, G. (2019). Text-mined dataset of inorganic materials synthesis recipes. Sci. data *6*, 203.

59. Weston, L., Tshitoyan, V., Dagdelen, J., Kononova, O., Trewartha, A., Persson, K.A., Ceder, G., and Jain, A. (2019). Named Entity Recognition and Normalization Applied to Large-Scale Information Extraction from the Materials Science Literature. J. Chem. Inf. Model. *59*, 3692–3702.

60. He, T., Sun, W., Huo, H., Kononova, O., Rong, Z., Tshitoyan, V., Botari, T., and Ceder, G. (2020). Similarity of Precursors in Solid-state Synthesis as Text-Mined from Scientific Literature. arXiv Prepr. arXiv2006, 10315.

61. Ong, S.P., Richards, W.D., Jain, A., Hautier, G., Kocher, M., Cholia, S., Gunter, D., Chevrier, V.L., Persson, K.A., and Ceder, G. (2013). Python Materials Genomics (pymatgen): A robust, open-source python library for materials analysis. Comput. Mater. Sci. *68*, 314–319.

62. Tran, T.T., Panella, J.R., Chamorro, J.R., Morey, J.R., and McQueen, T.M. (2017). Designing indirect-direct bandgap transitions in double perovskites. Mater. Horizons *4*, 688–693.

63. Du, K.Z., Meng, W., Wang, X., Yan, Y., and Mitzi, D.B. (2017). Bandgap Engineering of Lead-Free Double Perovskite $Cs_2AgBiBr_6$ through Trivalent Metal Alloying. Angew. Chemie - Int. Ed. *56*, 8158–8162.

64. Cao, X., Kang, L., Guo, S., Zhang, M., Lin, Z., and Gao, J. (2019). Cs_2NaVCl_6: A Pb-Free Halide Double Perovskite with Strong Visible and Near-Infrared Light Absorption. ACS Appl. Mater. Interfaces *11*, 38648–38653.

65. Pan, W., Wu, H., Luo, J., Deng, Z., Ge, C., Chen, C., Jiang, X., Yin, W., Niu, G., Zhu, L., et al. (2017). $Cs_2AgBiBr_6$ single-crystal X-ray detectors with a Low Detection Limit. Nat. Photonics *11*, 1–8.

66. Deng, W., Deng, Z.Y., He, J., Wang, M., Chen, Z.X., Wei, S.H., and Feng, H.J. (2017). Synthesis of $Cs_2AgSbCl_6$ and improved optoelectronic properties of $Cs_2AgSbCl_6/TiO_2$ heterostructure driven by the interface effect for lead-free double perovskites solar cells. Appl. Phys. Lett. *111*, 2–7.

67. Steele, J.A., Pan, W., Martin, C., Keshavarz, M., Debroye, E., Yuan, H., Banerjee, S., Fron, E., Jonckheere, D., Kim, C.W., et al. (2018). Photophysical Pathways in Highly Sensitive $Cs_2AgBiBr_6$ Double-Perovskite Single-Crystal X-Ray Detectors. Adv. Mater. *30*, 1–7.

68. Lozhkina, O.A., Murashkina, A.A., Elizarov, M.S., Shilovskikh, V. V., Zolotarev, A.A., Kapitonov, Y. V., Kevorkyants, R., Emeline, A. V., and Miyasaka, T. (2018). Microstructural analysis and optical properties of the halide double perovskite $Cs_2BiAgBr_6$ single crystals. Chem. Phys. Lett. *694*, 18–22.

69. Ji, F., Klarbring, J., Wang, F., Ning, W., Wang, L., Yin, C., Figueroa, J.S.M., Christensen, C.K., Etter, M., Ederth, T., et al. (2020). Lead-Free Halide Double Perovskite $Cs_2AgBiBr_6$ with Decreased Band Gap. Angew. Chemie - Int. Ed., 1–5.

70. Karmakar, A., Dodd, M.S., Agnihotri, S., Ravera, E., and Michaelis, V.K. (2018). Cu(II)-Doped $Cs_2SbAgCl_6$ Double Perovskite: A Lead-Free, Low-Bandgap Material. Chem. Mater. *30*, 8280–8290.

71. Kong, D., Cheng, D., Wang, X., Zhang, K., Wang, H., Liu, K., Li, H., Sheng, X., and Yin, L. (2020). Solution processed lead-free cesium titanium halide perovskites and their structural, thermal and optical characteristics. J. Mater. Chem. C *8*, 1591–1597.

72. Noculak, A., Noculak, A., Morad, V., Morad, V., McCall, K.M., McCall, K.M., Yakunin, S., Yakunin, S., Shynkarenko, Y., Shynkarenko, Y., et al. (2020). Bright Blue and Green

Luminescence of Sb(III) in Double Perovskite Cs_2MInCl_6(M = Na, K) Matrices. Chem. Mater. *32*, 5118–5124.

73. Arfin, H., Kaur, J., Sheikh, T., Chakraborty, S., and Nag, A. (2020). Bi^{3+}-Er^{3+} and Bi^{3+}-Yb^{3+} Codoped $Cs_2AgInCl_6$ Double Perovskite Near Infrared Emitters. Angew. Chemie - Int. Ed. *59*, 1–6.

74. Nila Nandha, K., and Nag, A. (2018). Synthesis and luminescence of Mn-doped $Cs_2AgInCl_6$ double perovskites. Chem. Commun. *54*, 5205–5208.

75. Wang, A., Yan, X., Zhang, M., Sun, S., Yang, M., Shen, W., Pan, X., Wang, P., and Deng, Z. (2016). Controlled synthesis of lead-free and stable perovskite derivative Cs_2SnI_6 nanocrystals via a facile hot-injection process. Chem. Mater. *28*, 8132–8140.

76. Creutz, S.E., Crites, E.N., Siena, M.C. De, and Gamelin, D.R. (2018). Colloidal Nanocrystals of Lead-Free Double-Perovskite (Elpasolite) Semiconductors: Synthesis and Anion Exchange To Access New Materials. Nano Lett. *6*, 1118–1123.

77. Dey, A., Richter, A.F., Debnath, T., Huang, H., Polavarapu, L., and Feldmann, J. (2020). Transfer of Direct to Indirect Bound Excitons by Electron Intervalley Scattering in $Cs_2AgBiBr_6$ Double Perovskite Nanocrystals. ACS Nano *14*, 5855–5861.

78. Zhu, D., Zito, J., Pinchetti, V., Dang, Z., Olivati, A., Pasquale, L., Tang, A., Za, M.L., Meinardi, F., Infante, I., et al. (2020). Compositional Tuning of Carrier Dynamics in $Cs_2Na_{1-x}AgxBiCl_6$ Double-Perovskite Nanocrystals. ACS Energy Lett. *5*, 1840–1847.

79. Wei, F., Deng, Z., Sun, S., Zhang, F., Evans, D.M., Kieslich, G., Tominaka, S., Carpenter, M.A., Zhang, J., Bristowe, P.D., et al. (2017). Synthesis and Properties of a Lead-Free Hybrid Double Perovskite: $(CH_3NH_3)_2AgBiBr_6$. Chem. Mater. *29*, 1089–1094.

80. Wei, F., Deng, Z., Sun, S., Xie, F., Kieslich, G., Evans, D.M., Carpenter, M.A., Bristowe, P.D., and Cheetham, A.K. (2016). The synthesis, structure and electronic properties of a lead-free hybrid inorganic-organic double perovskite $(MA)_2KBiCl_6$ (MA = methylammonium). Mater. Horizons *3*, 328–332.

81. Luo, J., Li, S., Wu, H., Zhou, Y., Li, Y., Liu, J., Li, J., Li, K., Yi, F., Niu, G., et al. (2018). $Cs_2AgInCl_6$ Double Perovskite Single Crystals: Parity Forbidden Transitions and Their Application for Sensitive and Fast UV Photodetectors. ACS Photonics *5*, 398–405.

82. Luo, J., Wang, X., Li, S., Liu, J., Guo, Y., Niu, G., Yao, L., Fu, Y., Gao, L., Dong, Q., et al. (2018). Efficient and stable emission of warm-white light from lead-free halide double perovskites. Nature *563*, 541–545.

83. Wei, F., Deng, Z., Sun, S., Hartono, N.T.P., Seng, H.L., Buonassisi, T., Bristowe, P.D., and Cheetham, A.K. (2019). Enhanced visible light absorption for lead-free double perovskite $Cs_2AgSbBr_6$. Chem. Commun. *55*, 3721–3724.

84. Zhang, C., Gao, L., Teo, S., Guo, Z., Xu, Z., Zhao, S., and Ma, T. (2018). Design of a novel and highly stable lead-free Cs_2NaBiI_6 double perovskite for photovoltaic application. Sustain. Energy Fuels *2*, 2419–2428.

85. Zhou, J., Rong, X., Zhang, P., Molokeev, M.S., Wei, P., Liu, Q., Zhang, X., and Xia, Z. (2019). Manipulation of Bi^{3+}/In^{3+} Transmutation and Mn^{2+}- Doping Effect on the Structure and Optical Properties of Double Perovskite Cs2NaBi1-xInxCl6. Adv. Opt. Mater. *7*, 1–9.

86. Tan, Z., Li, J., Zhang, C., Li, Z., Hu, Q., Xiao, Z., Kamiya, T., Hosono, H., Niu, G., Lifshitz, E., et al. (2018). Highly Efficient Blue-Emitting Bi-Doped Cs_2SnCl_6 Perovskite Variant: Photoluminescence Induced by Impurity Doping. Adv. Funct. Mater. *28*, 1801131.

87. Wang, M., Zeng, P., Bai, S., Gu, J., Li, F., Yang, Z., and Liu, M. (2018). High-Quality Sequential-Vapor-Deposited $Cs_2AgBiBr_6$ Thin Films for Lead-Free Perovskite Solar Cells. Sol. RRL *2*, 1800217.

88. Fan, P., Peng, H.-X., Zheng, Z.-H., Chen, Z.-H., Tan, S.-J., Chen, X.-Y., Luo, Y.-D., Su, Z.-H., Luo, I.-T., and Liang, G.-X. (2019). Single-Source Vapor-Deposited $Cs_2AgBiBr_6$ Thin Films for Lead-Free Perovskite Solar Cells. Nanomaterials, 1760.

89. Igbari, F., Wang, R., Wang, Z.K., Ma, X.J., Wang, Q., Wang, K.L., Zhang, Y., Liao, L.S., and Yang, Y. (2019). Composition Stoichiometry of $Cs_2AgBiBr_6$ Films for Highly Efficient Lead-Free Perovskite Solar Cells. Nano Lett. *19*, 2066–2073.

90. Longo, G., Mahesh, S., Buizza, L.R. V, Wright, A.D., Ramadan, A.J., Abdi-jalebi, M., Nayak, P.K., Herz, L.M., and Snaith, H.J. (2020). Understanding the Performance-Limiting Factors of $Cs_2AgBiBr_6$ Double-Perovskite Solar Cells.

91. Chen, M., Ju, M.G., Carl, A.D., Zong, Y., Grimm, R.L., Gu, J., Zeng, X.C., Zhou, Y., and Padture, N.P. (2018). Cesium Titanium(IV) Bromide Thin Films Based Stable Lead-free Perovskite Solar Cells. Joule *2*, 558–570.

92. Saparov, B., Sun, J., Meng, W., Xiao, Z., and Duan, H. (2016). Thin-Film Deposition and Characterization of a Sn-Deficient Perovskite Derivative Cs_2SnI_6. Chem. Mater. *28*, 2315–2322.

93. Ke, J.C.R., Lewis, D.J., Walton, A.S., Spencer, B.F., O'Brien, P., Thomas, A.G., and Flavell, W.R. (2018). Ambient-air-stable inorganic Cs_2SnI_6 double perovskite thin films: Via aerosol-assisted chemical vapour deposition. J. Mater. Chem. A *6*, 11205–11214.

94. Greul, E., Petrus, M.L., Binek, A., Docampo, P., and Bein, T. (2017). Highly stable, phase pure $Cs_2AgBiBr_6$ double perovskite thin films for optoelectronic applications. J. Mater. Chem. A *5*, 19972–19981.

95. Wu, C., Zhang, Q., Liu, Y., Luo, W., Guo, X., Huang, Z., Ting, H., Sun, W., Zhong, X., Wei, S., et al. (2018). The Dawn of Lead-Free Perovskite Solar Cell: Highly Stable Double Perovskite $Cs_2AgBiBr_6$ Film. Adv. Sci. *5*, 1700759.

96. Ning, W., Wang, F., Wu, B., Lu, J., Yan, Z., Liu, X., Tao, Y., Liu, J.M., Huang, W., Fahlman, M., et al. (2018). Long Electron–Hole Diffusion Length in High-Quality Lead-Free Double Perovskite Films. Adv. Mater. *30*, 1–6.

97. Hoye, R.L.Z., Eyre, L., Wei, F., Brivio, F., Sadhanala, A., Sun, S., Li, W., Zhang, K.H.L., MacManus-Driscoll, J.L., Bristowe, P.D., et al. (2018). Fundamental Carrier Lifetime Exceeding 1 µs in $Cs_2AgBiBr_6$ Double Perovskite. Adv. Mater. Interfaces *5*, 2–9.

98. Pantaler, M., Cho, K.T., Queloz, V.I.E., García Benito, I., Fettkenhauer, C., Anusca, I., Nazeeruddin, M.K., Lupascu, D.C., and Grancini, G. (2018). Hysteresis-Free Lead-Free Double-Perovskite Solar Cells by Interface Engineering. ACS Energy Lett. *3*, 1781–1786.

99. Lei, L.Z., Shi, Z.F., Li, Y., Ma, Z.Z., Zhang, F., Xu, T.T., Tian, Y.T., Wu, D., Li, X.J., and Du, G.T. (2018). High-efficiency and air-stable photodetectors based on lead-free double perovskite $Cs_2AgBiBr_6$ thin films. J. Mater. Chem. C *6*, 7982–7988.

100. Gao, W., Ran, C., Xi, J., Jiao, B., Zhang, W., Wu, M., Hou, X., and Wu, Z. (2018). High-Quality $Cs_2AgBiBr_6$ Double Perovskite Film for Lead-Free Inverted Planar Heterojunction Solar Cells with 2.2 % Efficiency. ChemPhysChem *19*, 1696–1700.

101. Weng, Z., Qin, J., Umar, A.A., Wang, J., Zhang, X., Wang, H., Cui, X., Li, X., Zheng, L., and Zhan, Y. (2019). Lead-Free $Cs_2BiAgBr_6$ Double Perovskite-Based Humidity Sensor with Superfast Recovery Time. Adv. Funct. Mater. *29*, 1–9.

102. Yang, J., Bao, C., Ning, W., Wu, B., Ji, F., Yan, Z., Tao, Y., Liu, J.M., Sum, T.C., Bai, S., et al. (2019). Stable, High-Sensitivity and Fast-Response Photodetectors Based on Lead-Free $Cs_2AgBiBr_6$ Double Perovskite Films. Adv. Opt. Mater. *7*, 1–8.

103. Ning, W., Zhao, X.G., Klarbring, J., Bai, S., Ji, F., Wang, F., Simak, S.I., Tao, Y., Ren, X.M., Zhang, L., et al. (2019). Thermochromic Lead-Free Halide Double Perovskites. Adv. Funct. Mater. *29*, 1–8.

104. Yang, X., Chen, Y., Liu, P., Xiang, H., Wang, W., Ran, R., Zhou, W., and Shao, Z. (2020). Simultaneous Power Conversion Efficiency and Stability Enhancement of $Cs_2AgBiBr_6$ Lead-Free Inorganic Perovskite Solar Cell through Adopting a Multifunctional Dye Interlayer. Adv. Funct. Mater., 2001557.

105. Yan, G., Jiang, B., Yuan, Y., Kuang, M., Liu, X., Zeng, Z., Zhao, C., He, J.H., and Mai, W. (2020). Importance of Bi-O Bonds at the $Cs_2AgBiBr_6$ Double-Perovskite/Substrate Interface for Crystal Quality and Photoelectric Performance. ACS Appl. Mater. Interfaces *12*, 6064–6073.

106. Lv, C., Yang, X., Shi, Z., Wang, L., Sui, L., Li, Q., Qin, J., Liu, K., Zhang, Z., Li, X., et al. (2020). Pressure-Induced Ultra-Broad-Band Emission of a $Cs_2AgBiBr_6$ Perovskite Thin Film. J. Phys. Chem. C *124*, 1732–1738.

107. Schmitz, A., Schaberg, L.L., Sirotinskaya, S., Pantaler, M., Lupascu, D.C., Benson, N., and Bacher, G. (2020). Fine Structure of the Optical Absorption Resonance in $Cs_2AgBiBr_6$ Double Perovskite Thin Films. ACS Energy Lett. *5*, 559–565.

108. Pai, N., Lu, J., Wang, M., Chesman, A.S.R., Seeber, A., Cherepanov, P. V., Senevirathna, D.C., Gengenbach, T.R., Medhekar, N. V., Andrews, P.C., et al. (2020). Enhancement of the intrinsic light harvesting capacity of $Cs_2AgBiBr_6$ double perovskite: Via modification with sulphide. J. Mater. Chem. A *8*, 2008–2020.

109. Zhang, Z., Wu, C., Wang, D., Liu, G., Zhang, Q., Luo, W., Qi, X., Guo, X., Zhang, Y., Lao, Y., et al. (2019). Improvement of $Cs_2AgBiBr_6$ double perovskite solar cell by rubidium doping. Org. Electron. *74*, 204–210.

110. Liu, Y., Zhang, L., Wang, M., Zhong, Y., Huang, M., Long, Y., and Zhu, H. (2019). Bandgap-tunable double-perovskite thin films by solution processing. Mater. Today *28*, 25–30.

111. Schwartz, D., Murshed, R., Larson, H., Usprung, B., Soltanmohamad, S., Pandey, R., Barnard, E.S., Rockett, A., Hartmann, T., Castelli, I.E., et al. (2020). Air Stable, High-Efficiency, Pt-Based Halide Perovskite Solar Cells with Long Carrier Lifetimes. Phys. Status Solidi - Rapid Res. Lett. *2000182*, 1–8.

112. Lee, B., Krenselewski, A., Baik, S. Il, Seidman, D.N., and Chang, R.P.H. (2017). Solution processing of air-stable molecular semiconducting iodosalts, $Cs_2SnI_{6-x}Br_x$, for potential solar cell applications. Sustain. Energy Fuels *1*, 710–724.

113. Dahl, J.C., Osowiecki, W.T., Cai, Y., Swabeck, J.K., Bekenstein, Y., Asta, M., Chan, E.M., and Alivisatos, A.P. (2019). Probing the Stability and Band Gaps of $Cs_2AgInCl_6$ and $Cs_2AgSbCl_6$ Lead-Free Double Perovskite Nanocrystals. Chem. Mater. *31*, 3134–3143.

114. Zhang, Z., Liang, Y., Huang, H., Liu, X., Li, Q., Chen, L., and Xu, D. (2019). Stable and Highly Efficient Photocatalysis with Lead-Free Double-Perovskite of $Cs_2AgBiBr_6$. Angew. Chemie - Int. Ed. *58*, 7263–7267.

115. Igbari, F., Wang, R., Wang, Z.K., Ma, X.J., Wang, Q., Wang, K.L., Zhang, Y., Liao, L.S., and Yang, Y. (2019). Composition Stoichiometry of $Cs_2AgBiBr_6$ Films for Highly Efficient Lead-Free Perovskite Solar Cells. Nano Lett. *19*, 2066–2073.

116. Wei, F., Deng, Z., Sun, S., Xie, F., Kieslich, G., Evans, D.M., Carpenter, M.A., Bristowe, P.D., Cheetham, A.K., Wei, F., et al. (2018). Lead-free halide double perovskite-polymer composites for flexible X-ray imaging. J. Mater. Chem. A *4*, 15031–15037.

117. Zhou, J., Xia, Z., Molokeev, M.S., Zhang, X., Peng, D., and Liu, Q. (2017). Composition design, optical gap and stability investigations of lead-free halide double perovskite $Cs_2AgInCl_6$. J. Mater. Chem. A *5*, 15031–15037.

118. Kibria, M.G., Zhao, S., Chowdhury, F.A., Wang, Q., Nguyen, H.P., Trudeau, M.L., Guo, H., and Mi, Z. (2014). Tuning the surface Fermi level on p-type gallium nitride nanowires for efficient overall water splitting. Nat Commun *5*, 3825.

119. Steele, J.A., Puech, P., Keshavarz, M., Yang, R., Banerjee, S., Debroye, E., Kim, C.W., Yuan, H., Heo, N.H., Vanacken, J., et al. (2018). Giant electron-phonon coupling and deep conduction band resonance in metal halide double perovskite. ACS Nano *12*, 8081–8090.

120. Filip, M.R., Hillman, S., Haghighirad, A.A., Snaith, H.J., and Giustino, F. (2016). Band Gaps of the Lead-Free Halide Double Perovskites $Cs_2BiAgCl_6$ and $Cs_2BiAgBr_6$ from Theory and Experiment. J. Phys. Chem. Lett. *7*, 2579–2585.

121. Xiao, Z., Meng, W., Wang, J., and Yan, Y. (2016). Thermodynamic Stability and Defect Chemistry of Bismuth-Based Lead-Free Double Perovskites. ChemSusChem *9*, 2628–2633.

122. Liu, M., Johnston, M.B., and Snaith, H.J. (2013). Efficient planar heterojunction perovskite solar cells by vapour deposition. Nature *501*, 395–398.

123. Li, X., Bi, D., Yi, C., Décoppet, J.D., Luo, J., Zakeeruddin, S.M., Hagfeldt, A., and Grätzel, M. (2016). A vacuum flash-assisted solution process for high-efficiency large-area perovskite solar cells. Science *353*, 58–62.

124. Kim, M., Kim, G.H., Oh, K.S., Jo, Y., Yoon, H., Kim, K.H., Lee, H., Kim, J.Y., and Kim, D.S. (2017). High-Temperature-Short-Time Annealing Process for High-Performance Large-Area Perovskite Solar Cells. ACS Nano *11*, 6057–6064.

125. Fan, P., Peng, H., Zheng, Z., Chen, Z., Tan, S., and Chen, X. (2019). Single-Source Vapor-Deposited $Cs_2AgBiBr_6$ Thin Films for Lead-Free Perovskite Solar Cells. *6*, 1–13.

126. Han, Q., Bai, Y., Liu, J., Du, K.Z., Li, T., Ji, D., Zhou, Y., Cao, C., Shin, D., Ding, J., et al. (2017). Additive engineering for high-performance room-temperature-processed perovskite absorbers with micron-size grains and microsecond-range carrier lifetimes. Energy Environ. Sci. *10*, 2365–2371.

127. Xiao, Z., Dong, Q., Bi, C., Shao, Y., Yuan, Y., and Huang, J. (2014). Solvent Annealing of Perovskite-Induced Crystal Growth for Photovoltaic-Device Efficiency Enhancement. Adv. Mater. *26*, 6503–6509.

128. Rao, H., Ye, S., Gu, F., Zhao, Z., Liu, Z., Bian, Z., and Huang, C. (2018). Morphology Controlling of All-Inorganic Perovskite at Low Temperature for Efficient Rigid and Flexible Solar Cells. Adv. Energy Mater. *8*, 1–8.

129. Nie, W., Tsai, H., Asadpour, R., Neukirch, A.J., Gupta, G., Crochet, J.J., Chhowalla, M., Tretiak, S., Alam, M.A., and Wang, H. (2015). High-efficiency solution-processed perovskite solar cells with millimeter-scale grains. Science *347*, 522–526.

130. Wang, Z., Liu, X., Lin, Y., Liao, Y., Wei, Q., Chen, H., Qiu, J., Chen, Y., and Zheng, Y. (2019). Hot-substrate deposition of all-inorganic perovskite films for low-temperature processed high-efficiency solar cells. J. Mater. Chem. A *7*, 2773–2779.

131. Luo, P., Liu, Z., Xia, W., Yuan, C., Cheng, J., and Lu, Y. (2015). Uniform, stable, and efficient planar-heterojunction perovskite solar cells by facile low-pressure chemical vapor deposition under fully open-air conditions. ACS Appl. Mater. Interfaces *7*, 2708–2714.

132. Li, Y., Cooper, J.K., Buonsanti, R., Giannini, C., Liu, Y., Toma, F.M., and Sharp, I.D. (2015). Fabrication of planar heterojunction perovskite solar cells by controlled low-pressure vapor annealing. J. Phys. Chem. Lett. *6*, 493–499.

133. Chiang, Y.H., Cheng, H.M., Li, M.H., Guo, T.F., and Chen, P. (2016). Low-Pressure Vapor-Assisted Solution Process for Thiocyanate-Based Pseudohalide Perovskite Solar Cells. ChemSusChem *9*, 2620–2627.

134. Bruening, K., and Tassone, C.J. (2018). Antisolvent processing of lead halide perovskite thin films studied by: In situ X-ray diffraction. J. Mater. Chem. A *6*, 18865–18870.

135. Jung, M., Ji, S.G., Kim, G., and Seok, S. Il (2019). Perovskite precursor solution chemistry: From fundamentals to photovoltaic applications. Chem. Soc. Rev. *48*, 2011–2038.

136. Prochowicz, D., Tavakoli, M.M., Solanki, A., Goh, T.W., Pandey, K., Sum, T.C., Saliba, M., and Yadav, P. (2018). Understanding the effect of chlorobenzene and isopropanol anti-solvent treatments on the recombination and interfacial charge accumulation in efficient planar perovskite solar cells. J. Mater. Chem. A *6*, 14307–14314.

137. Sakai, N., Pathak, S., Chen, H.W., Haghighirad, A.A., Stranks, S.D., Miyasaka, T., and Snaith, H.J. (2016). The mechanism of toluene-assisted crystallization of organic-inorganic perovskites for highly efficient solar cells. J. Mater. Chem. A *4*, 4464–4471.

138. Song, T.-B., Yuan, Z., Babbe, F., Nenon, D.P., Aydin, E., De Wolf, S., and Sutter-Fella, C.M. (2020). Dynamics of Antisolvent Processed Hybrid Metal Halide Perovskites Studied by In Situ Photoluminescence and Its Influence on Optoelectronic Properties . ACS Appl. Energy Mater. *3*, 2386–2393.

139. Jeon, N.J., Noh, J.H., Kim, Y.C., Yang, W.S., Ryu, S., and Seok, S. Il (2014). Solvent engineering for high-performance inorganic-organic hybrid perovskite solar cells. Nat. Mater. *13*, 897–903.

140. Xiao, M., Huang, F., Huang, W., Dkhissi, Y., Zhu, Y., Etheridge, J., Gray-Weale, A., Bach, U., Cheng, Y.B., and Spiccia, L. (2014). A fast deposition-crystallization procedure for highly efficient lead iodide perovskite thin-film solar cells. Angew. Chemie - Int. Ed. *53*, 9898–9903.

141. Xiao, M., Zhao, L., Geng, M., Li, Y., Dong, B., Xu, Z., Wan, L., Li, W., and Wang, S. (2018). Selection of an anti-solvent for efficient and stable cesium-containing triple cation planar perovskite solar cells. Nanoscale *10*, 12141–12148.

142. Slavney, A.H., Connor, B.A., Leppert, L., and Karunadasa, H.I. (2019). A pencil-and-paper method for elucidating halide double perovskite band structures. Chem. Sci. *10*, 11041–11053.

143. Faber, F.A., Lindmaa, A., Von Lilienfeld, O.A., and Armiento, R. (2016). Machine Learning Energies of 2 Million Elpasolite (ABC2D6) Crystals. Phys. Rev. Lett. *117*, 2–7.

144. Bartel, C.J., Sutton, C., Goldsmith, B.R., Ouyang, R., Musgrave, C.B., Ghiringhelli, L.M., and Scheffler, M. (2019). New tolerance factor to predict the stability of perovskite oxides and halides. Sci. Adv. *5*, 1–10.

145. Xiao, Z., and Yan, Y. (2017). Progress in Theoretical Study of Metal Halide Perovskite

Solar Cell Materials. Adv. Energy Mater. *7*.

146. Slavney, A.H., Leppert, L., Bartesaghi, D., Gold-Parker, A., Toney, M.F., Savenije, T.J., Neaton, J.B., and Karunadasa, H.I. (2017). Defect-Induced Band-Edge Reconstruction of a Bismuth-Halide Double Perovskite for Visible-Light Absorption. J. Am. Chem. Soc. *139*, 5015–5018.

147. Lindquist, K.P., Mack, S.A., Slavney, A.H., Leppert, L., Gold-Parker, A., Stebbins, J.F., Salleo, A., Toney, M.F., Neaton, J.B., and Karunadasa, H.I. (2019). Tuning the bandgap of $Cs_2AgBiBr_6$ through dilute tin alloying. Chem. Sci. *10*, 10620–10628.

148. Locardi, F., Sartori, E., Buha, J., Zito, J., Prato, M., Pinchetti, V., Zaffalon, M.L., Ferretti, M., Brovelli, S., Infante, I., et al. (2019). Emissive Bi-Doped Double Perovskite $Cs_2Ag_{1-x}Na_xInCl_6$ Nanocrystals. ACS Energy Lett. *4*, 1976–1982.

149. Sutter-Fella, C.M., Ngo, Q.P., Cefarin, N., Gardner, K.L., Tamura, N., Stan, C. V., Drisdell, W.S., Javey, A., Toma, F.M., and Sharp, I.D. (2018). Cation-Dependent Light-Induced Halide Demixing in Hybrid Organic-Inorganic Perovskites. Nano Lett. *18*, 3473–3480.

150. Hoke, E.T., Slotcavage, D.J., Dohner, E.R., Bowring, A.R., Karunadasa, H.I., and McGehee, M.D. (2015). Reversible photo-induced trap formation in mixed-halide hybrid perovskites for photovoltaics. Chem. Sci. *6*, 613–617.

151. Yang, B., Chen, J., Yang, S., Hong, F., Sun, L., Han, P., Pullerits, T., Deng, W., and Han, K. (2018). Lead-Free Silver-Bismuth Halide Double Perovskite Nanocrystals. Angew. Chemie *130*, 5457–5461.

152. Filip, M.R., Liu, X., Miglio, A., Hautier, G., and Giustino, F. (2018). Phase Diagrams and Stability of Lead-Free Halide Double Perovskites $Cs_2BB'X_6$: B = Sb and Bi, B′ = Cu, Ag, and Au, and X = Cl, Br, and I. J. Phys. Chem. C *122*, 158–170.

153. Pai, N., Lu, J., Gengenbach, T.R., Seeber, A., Chesman, A.S.R., Jiang, L., Senevirathna, D.C., Andrews, P.C., Bach, U., Cheng, Y.B., et al. (2019). Silver Bismuth Sulfoiodide Solar Cells: Tuning Optoelectronic Properties by Sulfide Modification for Enhanced Photovoltaic Performance. Adv. Energy Mater. *9*, 1–11.

154. Tang, G., Xiao, Z., and Hong, J. (2019). Designing Two-Dimensional Properties in Three-Dimensional Halide Perovskites via Orbital Engineering. J. Phys. Chem. Lett. *10*, 6688–6694.

155. Mao, L., Teicher, S.M.L., Stoumpos, C.C., Kennard, R.M., Decrescent, R.A., Wu, G., Schuller, J.A., Chabinyc, M.L., Cheetham, A.K., and Seshadri, R. (2019). Chemical and Structural Diversity of Hybrid Layered Double Perovskite Halides. J. Am. Chem. Soc. *141*, 19099–19109.

156. Bi, L.Y., Hu, Y.Q., Li, M.Q., Hu, T.L., Zhang, H.L., Yin, X.T., Que, W.X., Lassoued, M.S., and Zheng, Y.Z. (2019). Two-dimensional lead-free iodide-based hybrid double perovskites: Crystal growth, thin-film preparation and photocurrent responses. J. Mater. Chem. A *7*, 19662–19667.

157. Jana, M.K., Janke, S.M., Dirkes, D.J., Dovletgeldi, S., Liu, C., Qin, X., Gundogdu, K., You, W., Blum, V., and Mitzi, D.B. (2019). Direct-Bandgap 2D Silver-Bismuth Iodide Double Perovskite: The Structure-Directing Influence of an Oligothiophene Spacer Cation. J. Am. Chem. Soc. *141*, 7955–7964.

158. Fang, Y., Zhang, L., Wu, L., Yan, J., Lin, Y., Wang, K., Mao, W.L., and Zou, B. (2019). Pressure-Induced Emission (PIE) and Phase Transition of a Two-dimensional Halide Double Perovskite $(BA)_4AgBiBr_8$ ($BA=CH_3(CH_2)_3NH^{3+}$). Angew. Chemie *131*, 15393–

15397.

159. Xu, Z., Liu, X., Li, Y., Liu, X., Yang, T., Ji, C., Han, S., Xu, Y., Luo, J., and Sun, Z. (2019). Exploring Lead-Free Hybrid Double Perovskite Crystals of $(BA)_2CsAgBiBr_7$ with Large Mobility-Lifetime Product toward X-Ray Detection. Angew. Chemie *131*, 15904–15908.

160. Wang, C.F., Li, H., Li, M.G., Cui, Y., Son, X., Wang, Q.W., Jiang, J.Y., Hua, M.M., Xu, Q., Zhao, K., et al. (2021). Centimeter-Sized Single Crystals of Two-Dimensional Hybrid Iodide Double Perovskite (4,4-Difluoropiperidinium)$_4$AgBiI$_8$ for High-Temperature Ferroelectricity and Efficient X-Ray Detection. Adv. Funct. Mater. *2009457*, 1–8.

161. Guo, W., Liu, X., Han, S., Liu, Y., Xu, Z., Hong, M., Luo, J., and Sun, Z. (2020). Room-Temperature Ferroelectric Material Composed of a Two-Dimensional Metal Halide Double Perovskite for X-ray Detection. Angew. Chemie *132*, 13983–13988.

162. Li, Y., Yang, T., Xu, Z., Liu, X., Huang, X., Han, S., Liu, Y., Li, M., Luo, J., and Sun, Z. (2020). Dimensional Reduction of $Cs_2AgBiBr_6$: A 2D Hybrid Double Perovskite with Strong Polarization Sensitivity. Angew. Chemie *132*, 3457–3461.

163. Kulbak, M., Cahen, D., and Hodes, G. (2015). How Important Is the Organic Part of Lead Halide Perovskite Photovoltaic Cells? Efficient $CsPbBr_3$ Cells. J. Phys. Chem. Lett. *6*, 2452–2456.

164. Song, T. Bin, Yuan, Z., Mori, M., Motiwala, F., Segev, G., Masquelier, E., Stan, C. V., Slack, J.L., Tamura, N., and Sutter-Fella, C.M. (2019). Revealing the Dynamics of Hybrid Metal Halide Perovskite Formation via Multimodal In Situ Probes. Adv. Funct. Mater. *1908337*, 1–11.

165. Fu, L., Li, H., Wang, L., Yin, R., Li, B., and Yin, L. (2020). Defect passivation strategies in perovskites for an enhanced photovoltaic performance. Energy Environ. Sci. *13*, 4017–4056.

166. Yantara, N., Bhaumik, S., Yan, F., Sabba, D., Dewi, H.A., Mathews, N., Boix, P.P., Demir, H.V., and Mhaisalkar, S. (2015). Inorganic Halide Perovskites for Efficient Light-Emitting Diodes. J. Phys. Chem. Lett. *6*, 4360–4364.

167. Bai, D., Zhang, J., Jin, Z., Bian, H., Wang, K., Wang, H., Liang, L., Wang, Q., and Liu, S.F. (2018). Interstitial Mn^{2+}- Driven High-Aspect-Ratio Grain Growth for Low-Trap-Density Microcrystalline Films for Record Efficiency $CsPbI_2Br$ Solar Cells. ACS Energy Lett. *3*, 970–978.

168. Han, Y., Zhao, H., Duan, C., Yang, S., Yang, Z., Liu, Z., and Liu, S. (2020). Controlled n-Doping in Air-Stable $CsPbI_2Br$ Perovskite Solar Cells with a Record Efficiency of 16.79%. Adv. Funct. Mater. *30*, 1–8.

169. Ono, L.K., Juarez-Perez, E.J., and Qi, Y. (2017). Progress on Perovskite Materials and Solar Cells with Mixed Cations and Halide Anions. ACS Appl. Mater. Interfaces *9*, 30197–30246.

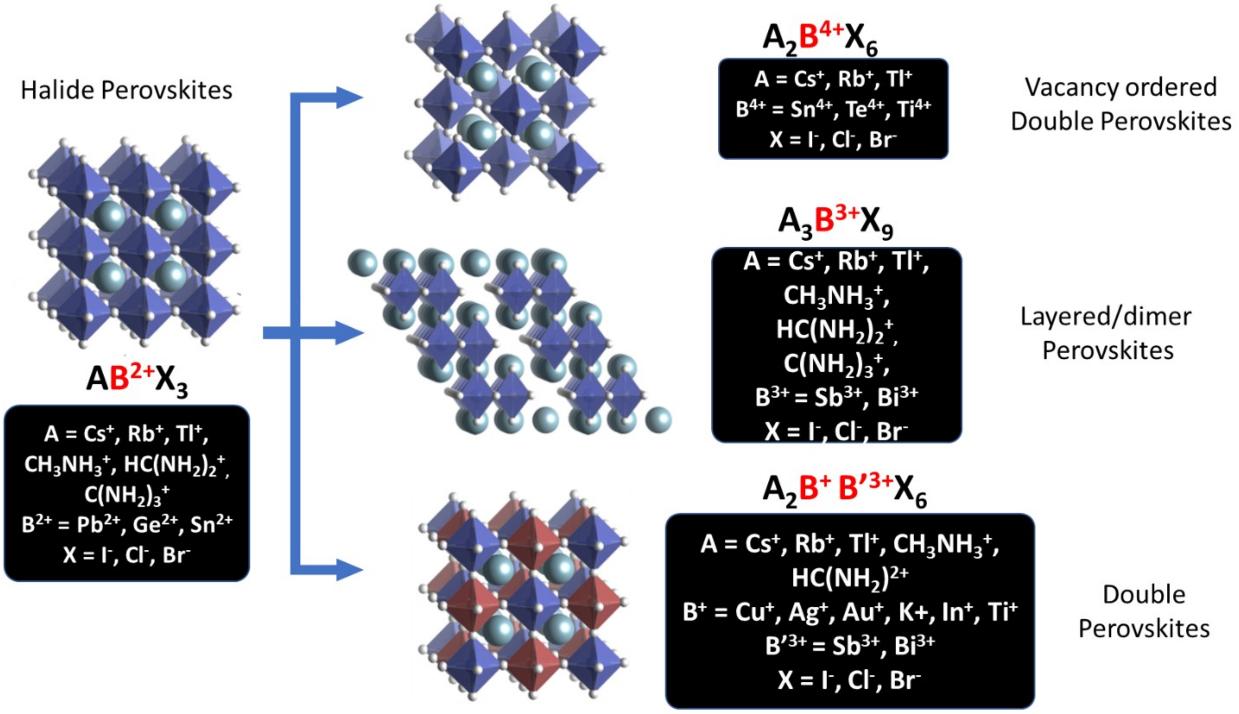

Figure 1. Schematic relation between the crystal structure of Pb halide perovskites with general formula ABX_3 and Pb-free perovskite derivatives falling into the categories of vacancy ordered double perovskites, layered/dimer perovskites, and double perovskites. Modified and reproduced with permission from Giustino et al.[28] and Chakraborty et al.[50] Copyright 2017, American Chemical Society.

A

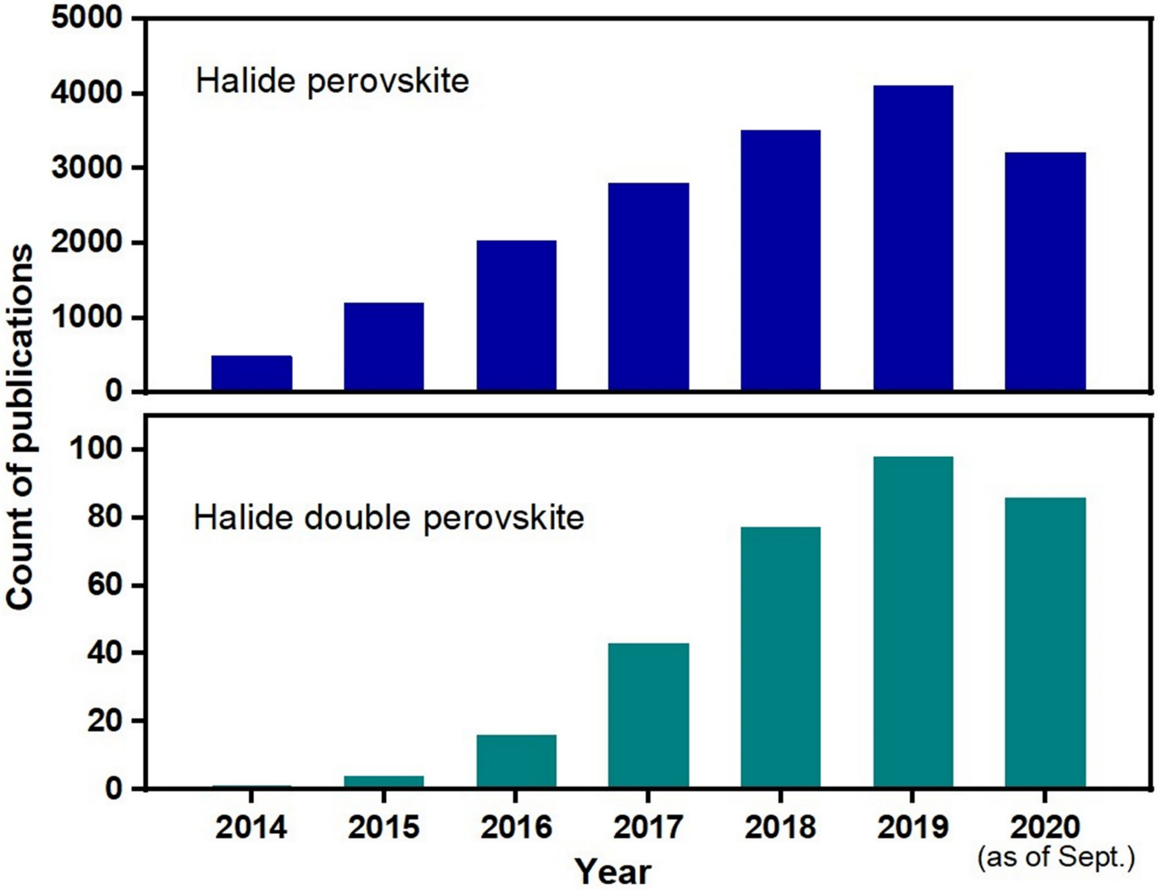

Halide perovskite
5000
4000
3000
2000
1000
0
Count of publications
Halide double perovskite
100
80
60
40
20
0
2014
2015
2016
2017
2018
2019
2020
(as of Sept.)
Year

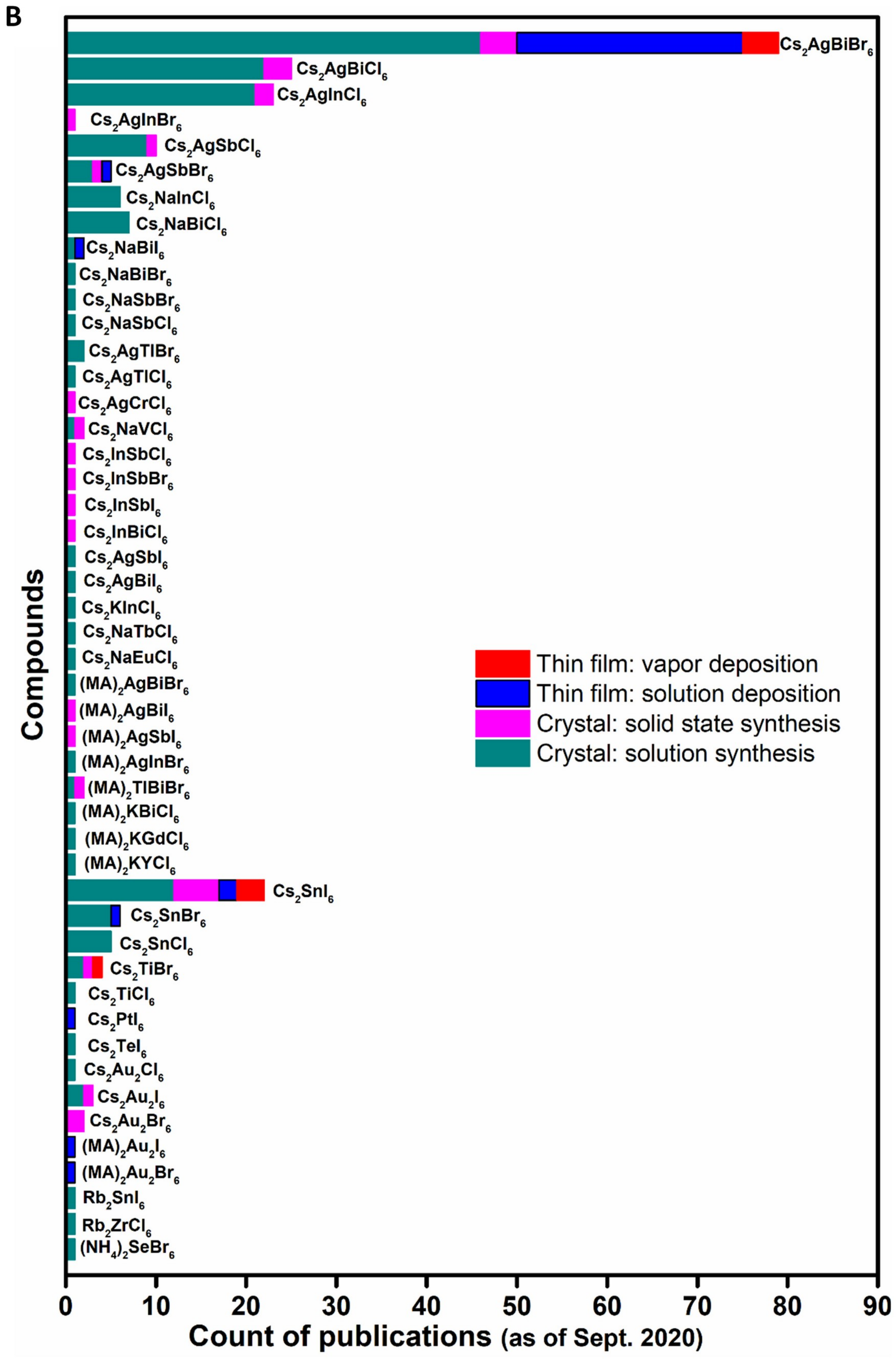
B
$Cs_2AgBiBr_6$
$Cs_2AgBiCl_6$
$Cs_2AgInCl_6$
$Cs_2AgInBr_6$
$Cs_2AgSbCl_6$
$Cs_2AgSbBr_6$
$Cs_2NaInCl_6$
$Cs_2NaBiCl_6$
Cs_2NaBiI_6
$Cs_2NaBiBr_6$
$Cs_2NaSbBr_6$
$Cs_2NaSbCl_6$
$Cs_2AgTlBr_6$
$Cs_2AgTlCl_6$
$Cs_2AgCrCl_6$
Cs_2NaVCl_6
$Cs_2InSbCl_6$
$Cs_2InSbBr_6$
Cs_2InSbI_6
$Cs_2InBiCl_6$
Cs_2AgSbI_6
Cs_2AgBiI_6
Cs_2KInCl_6
$Cs_2NaTbCl_6$
$Cs_2NaEuCl_6$
$(MA)_2AgBiBr_6$
$(MA)_2AgBiI_6$
$(MA)_2AgSbI_6$
$(MA)_2AgInBr_6$
$(MA)_2TlBiBr_6$
$(MA)_2KBiCl_6$
$(MA)_2KGdCl_6$
$(MA)_2KYCl_6$
Cs_2SnI_6
Cs_2SnBr_6
Cs_2SnCl_6
Cs_2TiBr_6
Cs_2TiCl_6
Cs_2PtI_6
Cs_2TeI_6
$Cs_2Au_2Cl_6$
$Cs_2Au_2I_6$
$Cs_2Au_2Br_6$
$(MA)_2Au_2I_6$
$(MA)_2Au_2Br_6$
Rb_2SnI_6
Rb_2ZrCl_6
$(NH_4)_2SeBr_6$
🟥 Thin film: vapor deposition
🟦 Thin film: solution deposition
🟪 Crystal: solid state synthesis
🟩 Crystal: solution synthesis
Compounds
0
10
20
30
40
50
60
70
80
90
Count of publications (as of Sept. 2020)

Figure 2. Text mining results from perovskite and double perovskite publications

(A) Number of publications on halide perovskites and halide double perovskites per year including experimental, theoretical, and review papers. The article extraction methodology is described in (B).

(B) Publication statistics for halide double perovskites synthesized by different methods. To mine for literature containing the synthesis of halide double perovskites, we used text mining techniques on full-text and abstracts from the materials science literature. We leveraged article data from a collection of full-text papers mined by the Ceder Group (with years ranging from 2000-2017)[58] and abstracts from MatScholar (with years ranging from 1900-2018)[59]. Articles from these databases were first filtered by a keyword search for "perovskite(s)". We then used Materials Entity Recognition[60] and formulae-analysis tools from Pymatgen (an open-source Python library for materials analysis)[61] to determine which of the article abstracts in these collections contained material entities with a character length greater than or equal to 7 and with a halide element whose stoichiometry was equal to 6, corresponding to the A2BB'X6 double perovskite structure. The articles from this subset were then inspected manually to ensure that they are indeed related to halide double perovskites. Then, we inspected these to confirm if halide double perovskites were synthesized and to determine which synthesis method was used. Articles from 2019-2020 were collected manually and from existing review literature[49] in this field. Finally, we supplemented our search with results from Clarivate Analytics' Web of Science literature search tool to account for any articles missing from the databases.

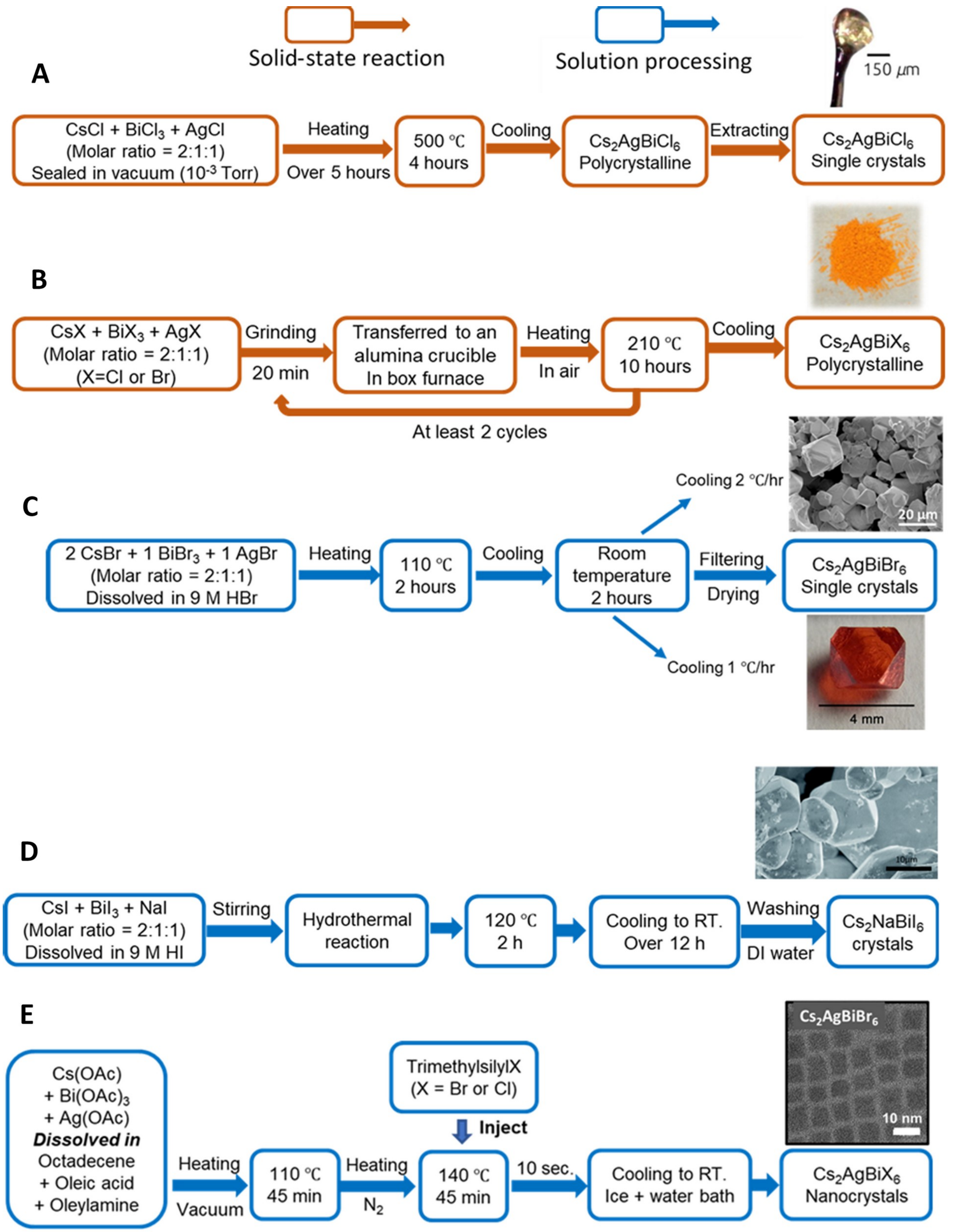

Figure 3. Flow schemes for the synthesis of halide double perovskite crystals via solid-state reaction (A-B) and via solution processing (C-E)

(A) Single crystal $Cs_2AgBiCl_6$[41,120], Reproduced with permissions from Volonakis et al.[41] and Filip et al.[120] Copyright 2016, American Chemical Society.
(B) Polycrystalline $Cs_2AgBiBr_6$ powder. Reproduced with permission from McClure et al.[44] Copyright 2016, American Chemical Society.
(C) Single crystal $Cs_2AgBiBr_6$. Reproduced with permission from Slavney et al.[43] Copyright 2016, American Chemical Society.
(D) Cs_2NaBiI_6 crystals (hydrothermal process). Reproduced with permission from Zhang et al.[84] Copyright 2018, Royal Society of Chemistry.
(E) Cs_2AgBiX_6 (X = Br or Cl) nanocrystals. Reproduced with permission from Creutz et al.[76] Copyright 2018, American Chemical Society.

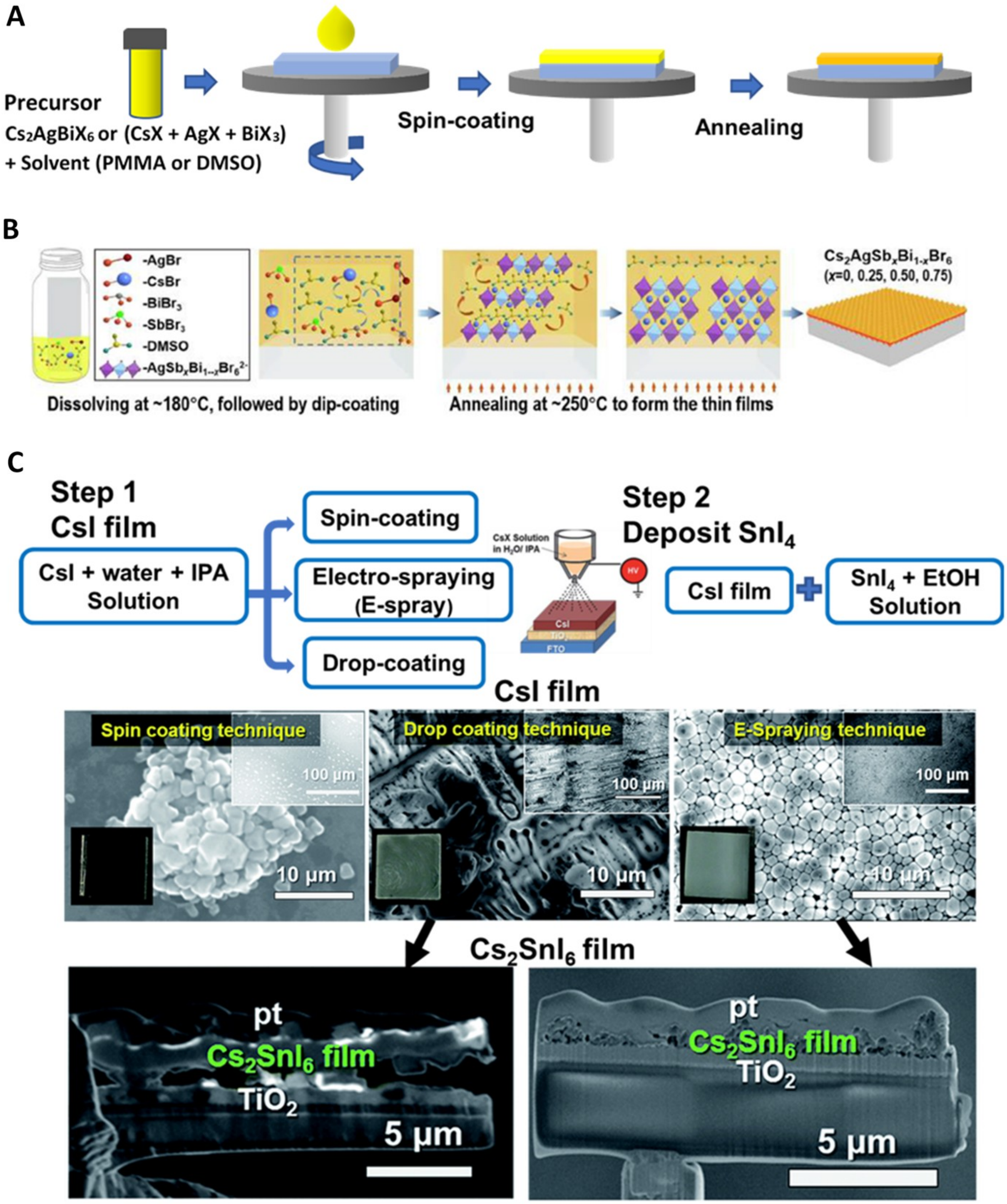

Figure 4. Double perovskite thin films synthesized via solution deposition

(A) Single step spin-coating deposition. Reproduced with permission from Igbari et al.[115] Copyright 2019, American Chemical Society.

(B) $Cs_2AgSb_xBi_{1-x}Br_6$ film prepared via dip-coating. Reproduced with permission from Liu et al.[110] Copyright 2019, Elsevier.

(C) Cs_2SnI_6 thin film prepared via a two-step solution synthesis method. Reproduced with permission from Lee et al.[112] Copyright 2017, Royal Society of Chemistry.

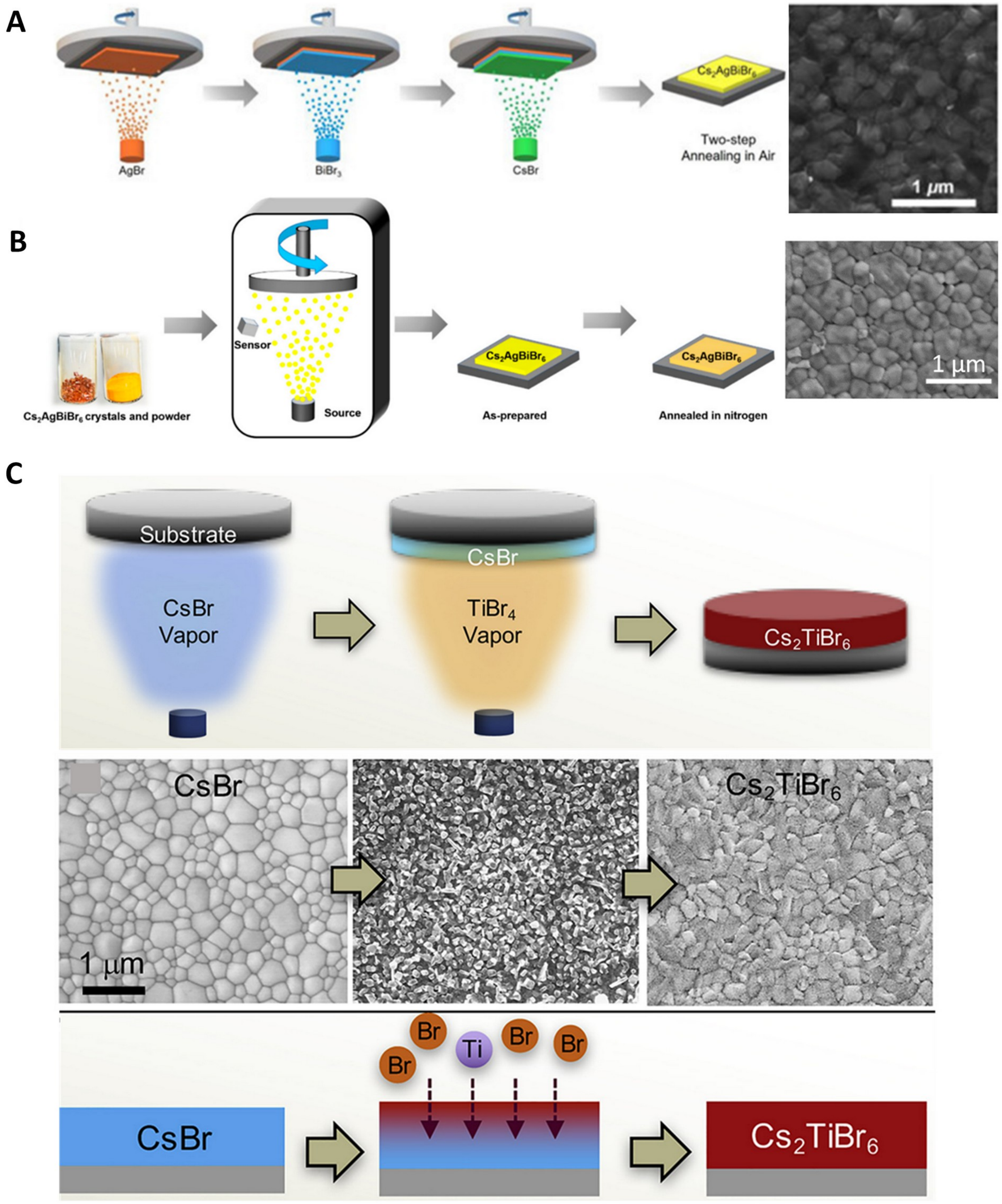

Figure 5. Double perovskite thin films synthesized via vacuum-based vapor deposition.
(A) $Cs_2AgBiBr_6$ thin film synthesized via a sequential vapor deposition started with AgBr, $BiBr_3$ and CsBr solids. Reproduced with permission from Wang et al.[87] Copyright 2018, John Wiley & Sons, Inc.

(B) Single-source vacuum vapor deposition from $Cs_2AgBiBr_6$ crystals. Reproduced from Fan et al.[88] Copyright 2019, MDPI.
(C) Two-step vapor deposition of Cs_2TiBr_6 starting with a thermally evaporated CsBr film followed by annealing in $TiBr_4$ vapor. Reproduced with permission from Chen et al.[91] Copyright 2018, Elsevier.

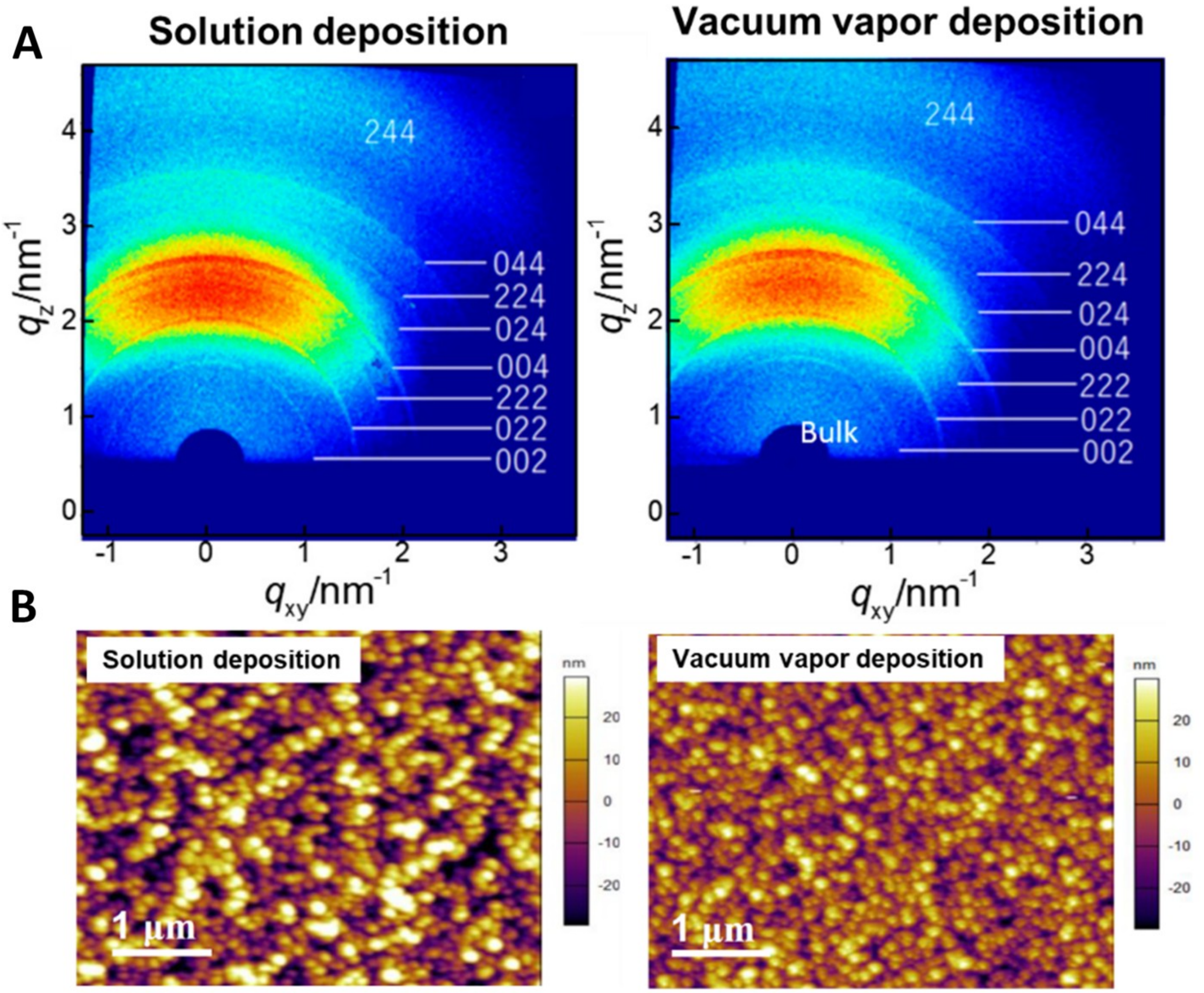

Figure 6. Film quality comparison between solution and vacuum deposited films by (A) GIXRD and (B) AFM. Reproduced with permission from Igbari et al.[115] Copyright 2019, American Chemical Society.

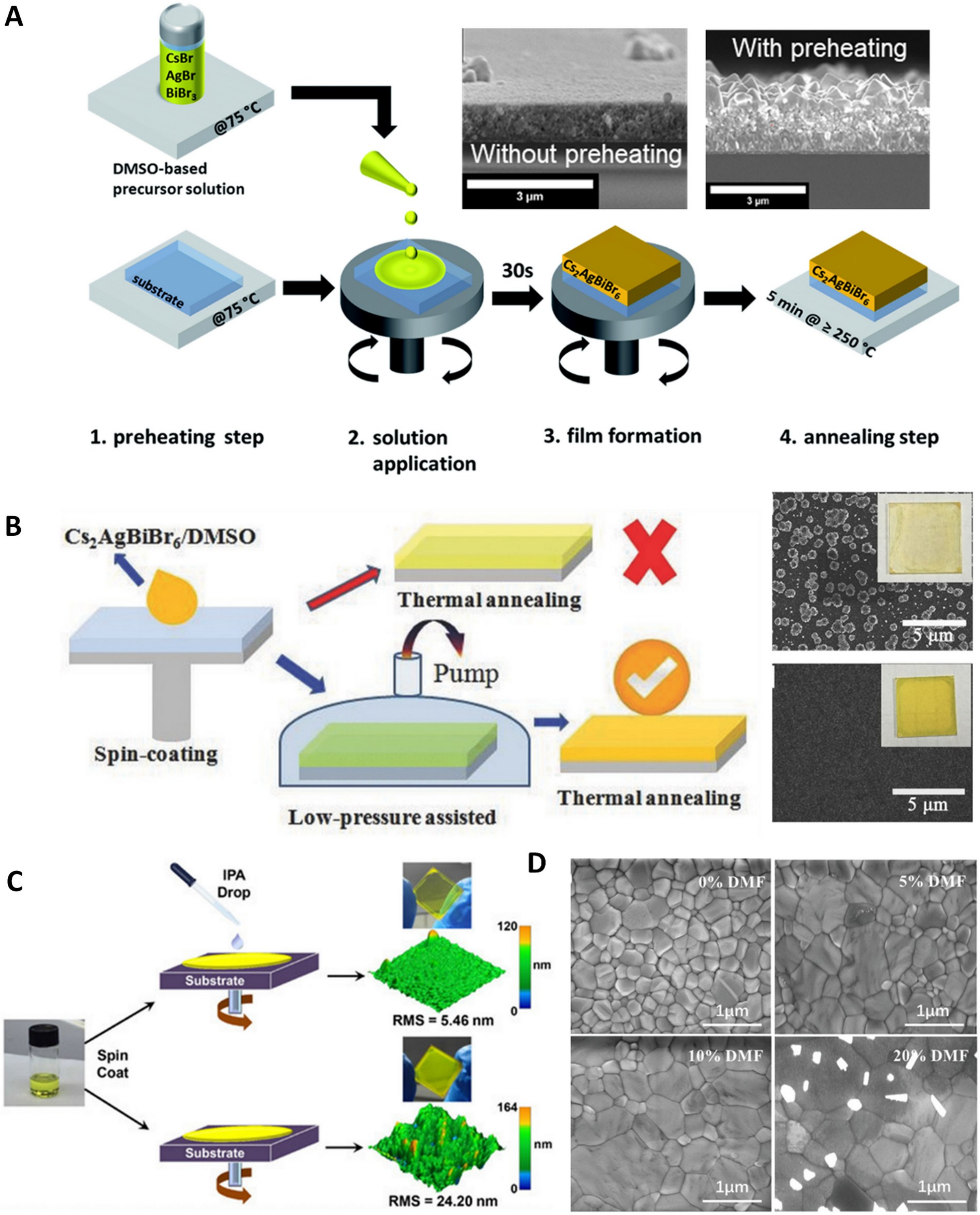

Figure 7. Modifications of the solution deposition process

(A) Substrate and precursor preheating. Reproduced with permission from Greul et al.[94] Copyright 2017, Royal Society of Chemistry.

(B) Low-pressure assisted solution deposition. Reproduced from Wu et al.[95] Copyright 2018, John Wiley & Sons, Inc.
(C) Antisolvent (IPA) dropping during spin-coating. Reproduced with permission from Gao et al.[100] Copyright 2018, John Wiley & Sons, Inc.
(D) SEM images of $Cs_2AgBiBr_6$ films fabricated from mixed DMF/DMSO solutions. Reproduced with permission from Yang et al.[102] Copyright 2019, John Wiley & Sons, Inc.

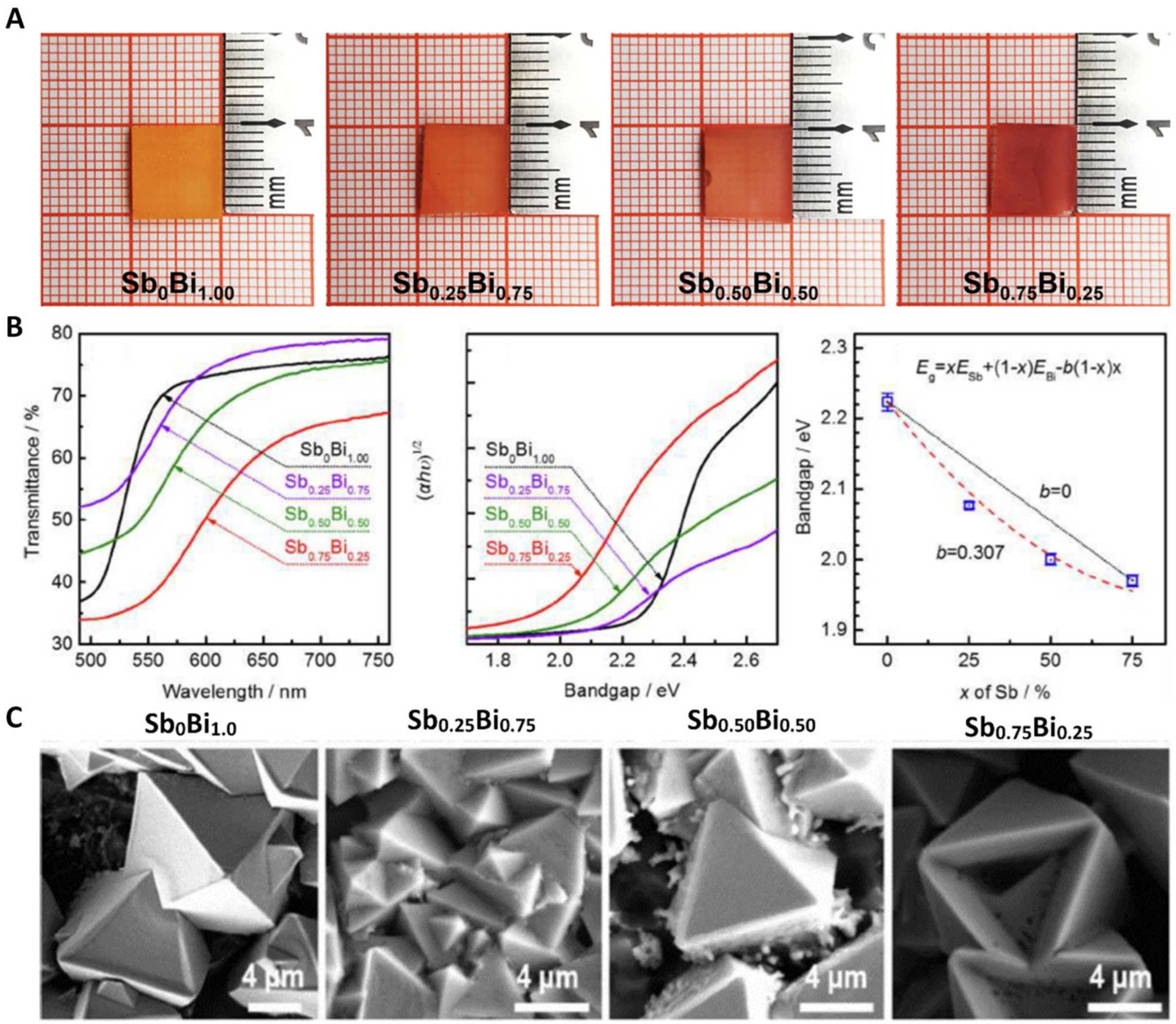

Figure 8. (A) Optical images, (B) Optical properties and (C) SEM images of $Cs_2AgSb_xBi_{1-x}Br_6$ (x = 0, 0.25, 0.50, 0.75) thin films. Reproduced with permission from Liu et al.[110] Copyright 2019, Elsevier.

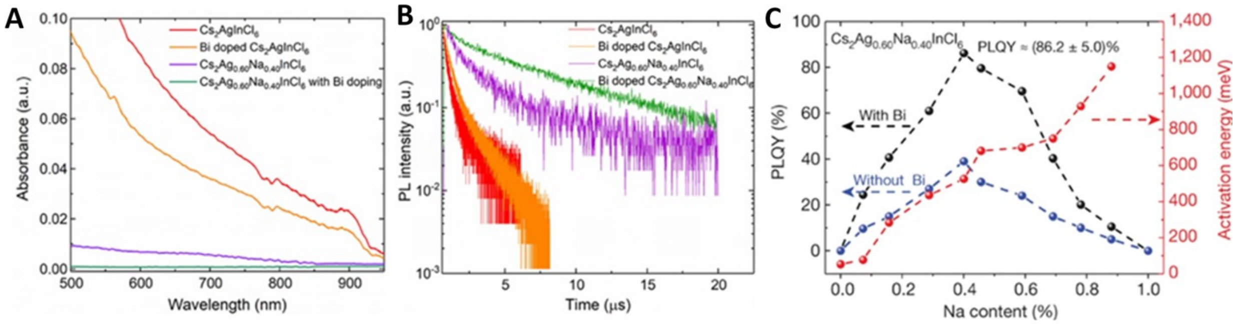

Figure 9. (A) Absorption spectra, (B) PL lifetime, and (C) Activation energy and photoluminescence quantum yield (PLQY) of Bi-doped $Cs_2Ag_xNa_{1-x}InCl_6$. Reproduced with permission from Luo et al.[82] Copyright 2018, Nature Publishing Group.

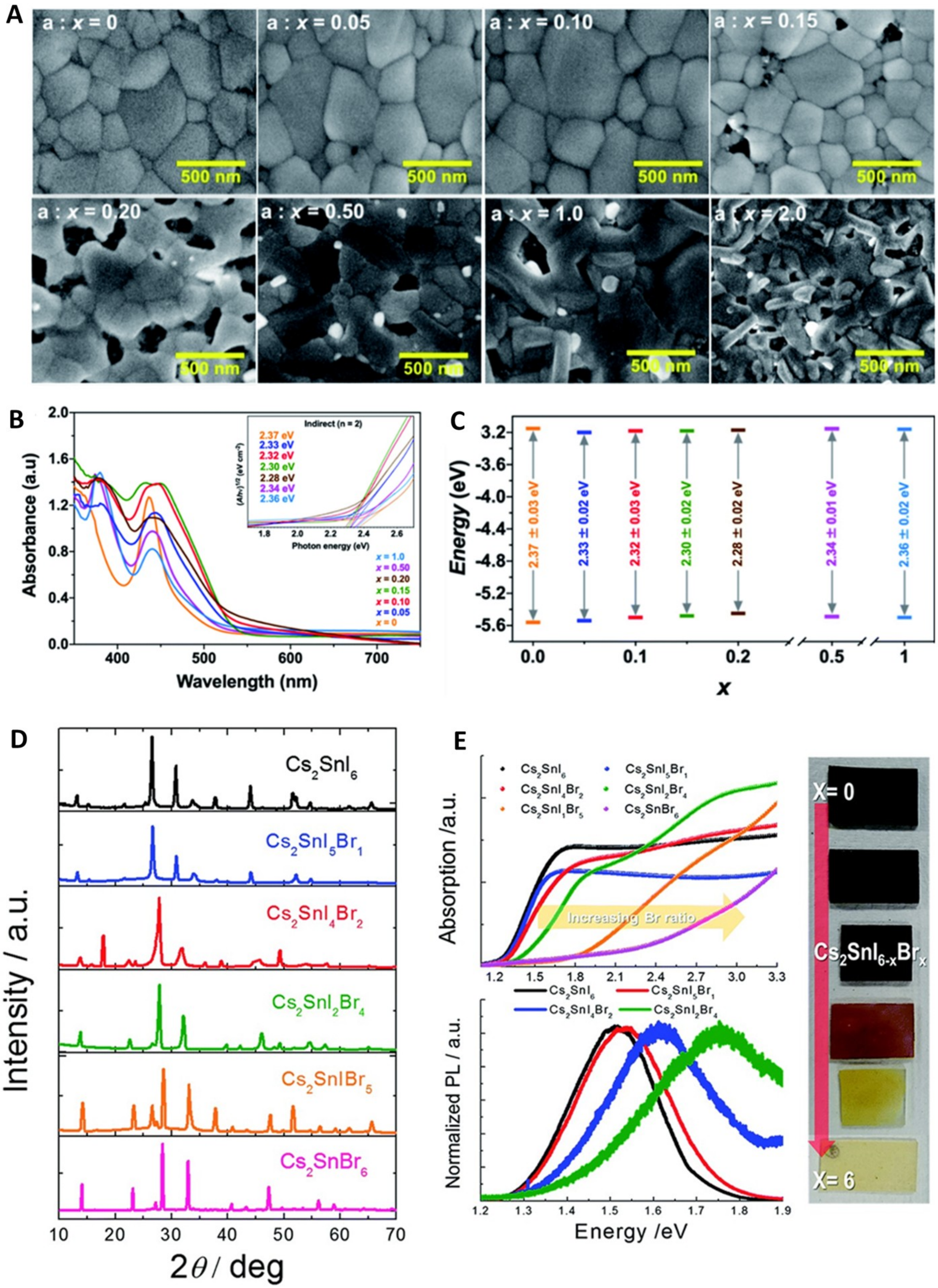
A
a : x = 0
a : x = 0.05
a : x = 0.10
a : x = 0.15
a : x = 0.20
a : x = 0.50
a : x = 1.0
a : x = 2.0
500 nm
B
Absorbance (a.u)
Wavelength (nm)
2.0
1.6
1.2
0.8
0.4
0.0
400
500
600
700
Indirect (n = 2)
2.37 eV
2.33 eV
2.32 eV
2.30 eV
2.28 eV
2.34 eV
2.36 eV
$(Ah\nu)^{1/2}$ (eV cm^{-2})
1.8
2.0
2.2
2.4
2.6
Photon energy (eV)
x = 1.0
x = 0.50
x = 0.20
x = 0.15
x = 0.10
x = 0.05
x = 0
C
Energy (eV)
3.2
-3.6
-4.0
-4.4
-4.8
-5.2
-5.6
2.37 ± 0.03 eV
2.33 ± 0.02 eV
2.32 ± 0.03 eV
2.30 ± 0.02 eV
2.28 ± 0.02 eV
2.34 ± 0.01 eV
2.36 ± 0.02 eV
0.0
0.1
0.2
0.5
1
x
D
Cs_2SnI_6
$Cs_2SnI_5Br_1$
$Cs_2SnI_4Br_2$
$Cs_2SnI_2Br_4$
Cs_2SnIBr_5
Cs_2SnBr_6
Intensity / a.u.
2θ / deg
10
20
30
40
50
60
70
E
Cs_2SnI_6
$Cs_2SnI_5Br_1$
$Cs_2SnI_4Br_2$
$Cs_2SnI_2Br_4$
$Cs_2SnI_1Br_5$
Cs_2SnBr_6
Absorption /a.u.
Increasing Br ratio
1.2
1.5
1.8
2.1
2.4
2.7
3.0
3.3
Cs_2SnI_6
$Cs_2SnI_5Br_1$
$Cs_2SnI_4Br_2$
$Cs_2SnI_2Br_4$
Normalized PL / a.u.
1.2
1.3
1.4
1.5
1.6
1.7
1.8
1.9
Energy /eV
X= 0
$Cs_2SnI_{6-x}Br_x$
X= 6

Figure 10. Effects of compositional engineering

(A) Effect of sulphide modification on morphology, (B) bandgap, and (C) electronic band alignment of $Cs_2AgBiBr_{6-2x}S_x$ thin films. Reproduced with permission from Pai et al.[108] Copyright 2020, Royal Society of Chemistry.

(D) XRD patterns and (E) absorption and PL spectra of $Cs_2SnI_{6-x}Br_x$ thin films synthesized by the two-step solution process. Reproduced with permission from Lee et al.[112] Copyright 2017, Royal Society of Chemistry.

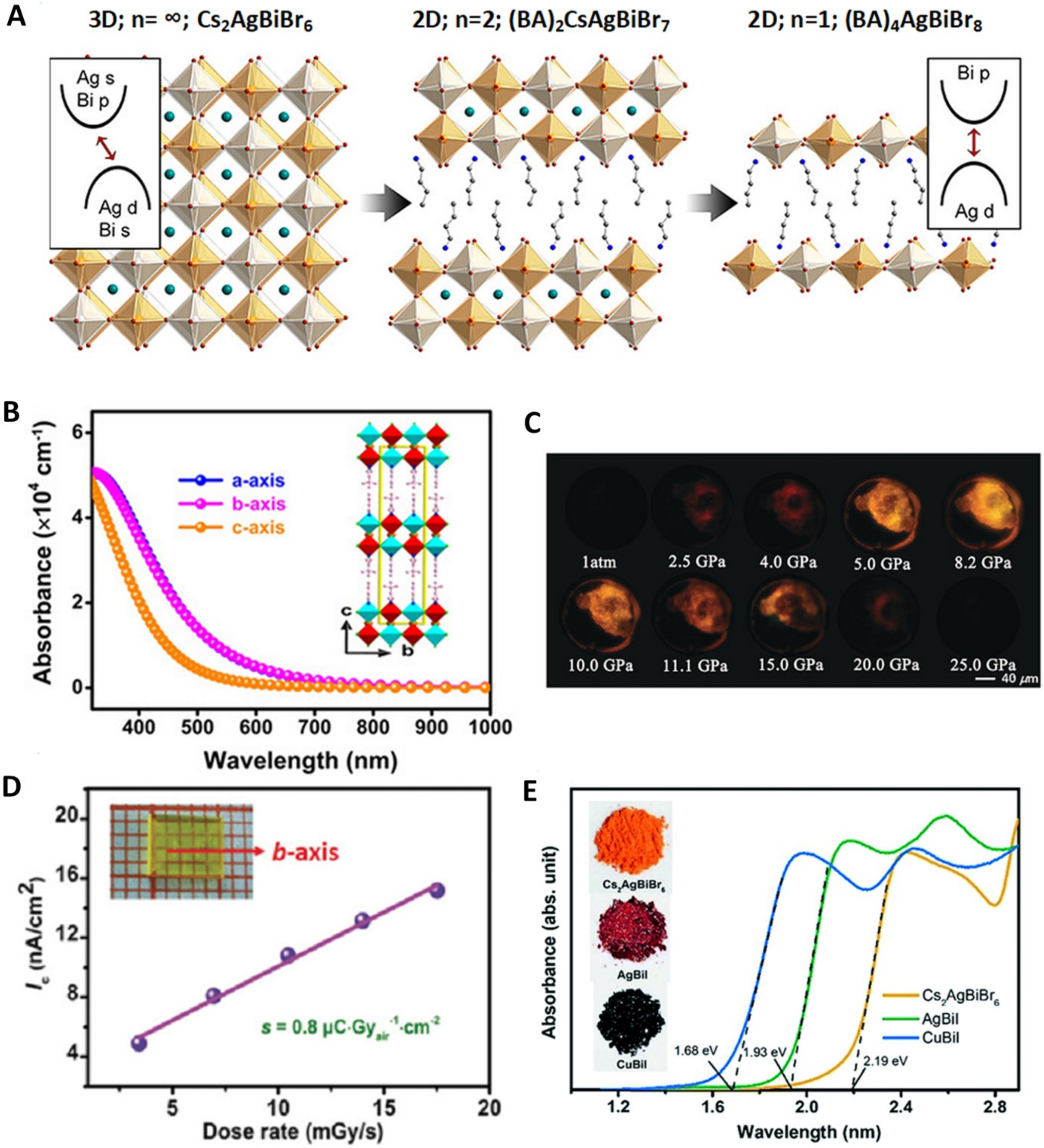

Figure 11. Dimensional reduction of double perovskites

(A) Schematic representation of the evolution of the 3D double perovskite structure to 2D layered double perovskite structure. Modified and reproduced with permission from Connor et al.[51] Copyright 2018, American Chemical Society.
(B) Anisotropy of optical absorbance of $(i\text{-}PA)_2CsAgBiBr_7$ (i-PA=isopentylammonium) along the three crystallographic axes. Reproduced with permission from Li et al.[162] Copyright 2020, John Wiley & Sons, Inc.
(C) PL micrographs showing pressure-induced emission at different pressure for $(BA)_4AgBiBr_8$. Reproduced with permission from Fang et al.[158] Copyright 2019, John Wiley & Sons, Inc.
(D) Photocurrent generated by X-ray irradiation with various dose rates (at 10 V) for $(CPA)_4AgBiBr_8$. Reproduced with permission from Guo et al.[161] Copyright 2020, John Wiley & Sons, Inc.
(E) Absorbance spectra of $Cs_2AgBiBr_6$, $(NH_3C_6H_{10}NH_3^{+2})_2AgBiI_8\cdot H_2O$ (=AgBiI), and $(C_6H_{16}N_2)_2CuBiI_8\cdot 0.5H_2O$ (=CuBiI). Reproduced with permission from Bi et al.[156] Copyright 2019, Royal Society of Chemistry.